© 2021. Published by The Company of Biologists Ltd | Development (2021) 148, dev199591. doi:10.1242/dev.199591

RESEARCH ARTICLE

Trp53 ablation fails to prevent microcephaly in mouse pallium with impaired minor intron splicing

Alisa K. White[1,*], Marybeth Baumgartner[2,*], Madisen F. Lee[1], Kyle D. Drake[1], Gabriela S. Aquino[1] and Rahul N. Kanadia[1,3,‡]

ABSTRACT

Minor spliceosome inhibition due to mutations in *RNU4ATAC* are linked to primary microcephaly. Ablation of *Rnu11*, which encodes a minor spliceosome snRNA, inhibits the minor spliceosome in the developing mouse pallium, causing microcephaly. There, cell cycle defects and p53-mediated apoptosis in response to DNA damage resulted in loss of radial glial cells (RGCs), underpinning microcephaly. Here, we ablated *Trp53* to block cell death in *Rnu11* cKO mice. We report that *Trp53* ablation failed to prevent microcephaly in these double knockout (dKO) mice. We show that the transcriptome of the dKO pallium was more similar to the control compared with the *Rnu11* cKO. We find aberrant minor intron splicing in minor intron-containing genes involved in cell cycle regulation, resulting in more severely impaired mitotic progression and cell cycle lengthening of RGCs in the dKO that was detected earlier than in the *Rnu11* cKO. Furthermore, we discover a potential role of p53 in causing DNA damage in the developing pallium, as detection of γH2aX+ was delayed in the dKO. Thus, we postulate that microcephaly in minor spliceosome-related diseases is primarily caused by cell cycle defects.

KEY WORDS: Cortical development, Microcephaly, Cell cycle, Minor spliceosome, U11 snRNA

INTRODUCTION

The complex higher-order functions carried out by the cortex, such as controlling motor and sensory functions as well as perception, thought and memory, depend on a complex neuronal architecture (Douglas et al., 1995). The cortex consists of a vast number of diverse neuronal subtypes that must be present in the right proportion, be correctly laminated and form the appropriate synaptic partners. Thus, proper cortical function requires proper cortical development. Early brain development requires a precise balance of progenitor cell amplification and neurogenesis, placing cell cycle regulation at the core of cortical development and disease (Dehay and Kennedy, 2007). Indeed, a range of sources, including environmental factors such as maternal exposure to toxins and pathogens, have been linked to disruption in cell cycle and cortical development (Chen et al., 2003; Feldman et al., 2012; von der Hagen et al., 2014; Rasmussen et al., 2016). Consequently, proliferation defects and too few progenitor cells often manifests as primary microcephaly in humans.

Mutations in genes involved in cell cycle regulation that result in microcephaly in humans provide insight into the cellular and molecular processes essential for cortical development (von der Hagen et al., 2014). Among the genes linked to microcephaly, more than half encode proteins localizing to the centrosome and are vital for centriole biogenesis and duplication (Jayaraman et al., 2018). Therefore, disruptions of functions encoded by such genes would result in centrosome dysfunction, often manifesting in impaired chromosome segregation and other mitotic defects. Furthermore, many genes involved in DNA replication and cell cycle checkpoints have been associated with microcephaly, highlighting the importance of cell cycle regulation for proper cortical development (Jayaraman et al., 2018).

Rare forms of primary microcephaly are linked to mutations in *RNU4ATAC*, which encodes the U4atac small nuclear RNA (snRNA), an essential component of the minor spliceosome. This disruption results in a spectrum of diseases including microcephalic osteodysplastic primordial dwarfism type 1 (MOPD1), Lowry-Wood syndrome (LWS), and Roifman syndrome (RS) (Edery et al., 2011; He et al., 2011; Merico et al., 2015; Farach et al., 2018). Despite the variability in the symptoms observed in these patients, microcephaly is common to all, which reveals the significance of the minor spliceosome in cortical development. The minor spliceosome, consisting of U11, U12, U4atac, U6atac and U5 snRNAs and associated proteins, is responsible for the removal of less than 0.5% of all introns, termed minor introns, found in ∼700 genes in humans (Levine and Durbin, 2001; Patel and Steitz, 2003; Olthof et al., 2019). Minor intron-containing genes (MIGs) perform disparate functions, ranging from transcription factors and splicing factors to protein kinases, translation regulators, ion channels and others (Burge et al., 1998; Baumgartner et al., 2019). As such, disruption of minor intron splicing would result in a large molecular footprint, and it is therefore difficult to determine the precise molecular defect that drives microcephaly in these patients. We have previously leveraged our conditional knockout (cKO) mouse targeting *Rnu11*, which encodes the U11 snRNA, to model microcephaly in these patients and study the molecular and cellular defects underpinning cortical defects in these diseases (Baumgartner et al., 2018). We have reported that *Emx1*-Cre-mediated ablation of *Rnu11* resulted in microcephaly at birth, which was caused by simultaneous cell cycle defects and cell death of radial glial cells (RGCs) in the U11-null developing cortex (Baumgartner et al., 2018).

Here, we test the hypothesis that the primary defects driving microcephaly in the U11-null developing cortex are cell cycle defects, which are upstream of the cell death phenotype. Several mouse models of microcephaly, including *Sas4* (Bazzi and Anderson, 2014; Insolera et al., 2014), *Kif20b* (Janisch et al., 2013; Little and Dwyer, 2019) and *Magoh* (Silver et al., 2010; Mao et al.,

[1]Physiology and Neurobiology Department, University of Connecticut, Storrs, CT 06269, USA. [2]Department of Genetics, Yale School of Medicine, New Haven, CT 06510, USA. [3]Institute of Systems Genomics, University of Connecticut, Storrs, CT 06269, USA.
*These authors contributed equally to this work

‡Author for correspondence (rahul.kanadia@uconn.edu)

K.D.D., 0000-0001-5615-9916; R.N.K., 0000-0001-7197-912X

Handling Editor: Paola Arlotta
Received 5 March 2021; Accepted 17 September 2021

Development (2021) 148, dev199591. doi:10.1242/dev.199591

2016), display cell cycle defects and p53-mediated cell death. Microcephaly in these mouse models can be rescued through ablation of *Trp53*, which encodes the protein p53. Given that we also observed cell cycle defects and p53-mediated apoptosis in the U11-null pallium, we sought to prevent cell death by ablating *Trp53* in the *Rnu11* cKO mouse to generate double knockout (dKO) mice. This allowed us to block apoptosis in the U11-null pallium and study both the progression of DNA damage and cell cycle defects triggered by minor spliceosome disruption and the relative contribution of these defects to microcephaly.

Here, we report that blocking p53-mediated cell death still resulted in primary microcephaly in the dKO mice. This, combined with the fact that cell cycle defects were detected earlier and were more severe in the dKO, compared with the *Rnu11* cKO, suggests that microcephaly observed in minor spliceosome disease is primarily driven by cell cycle defects. Specifically in the dKO, RGCs experience elongated prometaphase and there are fewer RGCs in S-phase. We found a significant increase in the overall cell cycle length, driven primarily by lengthening of G1 and/or G2 phases. Importantly, we identified the primary molecular defect of elevated minor intron retention in the dKO, which was similar to that seen in the *Rnu11* cKO. We also observed elevated alternative splicing (AS) across minor introns in both the *Rnu11* cKO and dKO developing cortices, which is consistent with our recent report (Olthof et al., 2021). Based on current literature and previous observations in the *Rnu11* cKO pallium, we anticipated that accumulation of DNA damage, which is thought to activate p53 stabilization, would be detected in the dKO (Lakin and Jackson, 1999; Cheng and Chen, 2010). Surprisingly, DNA damage was delayed in the dKO, relative to the *Rnu11* cKO. This finding suggests that, in the developing U11-null pallium, p53 might not only respond to DNA damage, but might also participate in DNA damage. In all, we have uncovered that microcephaly in minor spliceosome disease is driven primarily by cell cycle defects, predominantly those affecting mitotic progression.

RESULTS

Ablation of p53 in *Rnu11* cKO does not prevent microcephaly

We have previously shown that ablation of U11 results in minor intron splicing defects that cause cell cycle defects and DNA damage, which together lead to p53-mediated apoptosis of RGCs, resulting in microcephaly in the *Rnu11* cKO (Fig. 1A) (Baumgartner et al., 2018). To block cell death, we ablated *Trp53* in the *Rnu11* cKO mice to produce mice with the following genotypes: *Rnu11*$^{WT/Flx}$::Trp53$^{WT/WT}$::*Emx1*-Cre^{+} (control), *Rnu11*$^{Flx/Flx}$::*Trp53*$^{WT/WT}$::*Emx1*-Cre^{+} (*Rnu11* cKO), and *Rnu11*$^{Flx/Flx}$::*Trp53*$^{Flx/Flx}$::*Emx1*-Cre^{+} (dKO) mice (Fig. 1B). At birth, we observed microcephaly in the dKO mice (Fig. 1C), which was confirmed by cortical weight measurements (Fig. 1D). To further quantify the cortical phenotype present at P0, we employed a strategy which included three parameters: hemi-cortical surface area, anterior-posterior length and cortical length (Fig. 1E, top panel) (Ka et al., 2021). We found a significant reduction in hemi-cortical surface area, anterior-posterior length and cortical length the *Rnu11* cKO and dKO relative to the control, with no significant change between the *Rnu11* cKO and dKO (Fig. 1E, bottom panel). P0 coronal brain sections from each genotype stained with Nissl in the rostral to caudal axis showed reductions in cortical thickness in both the *Rnu11* cKO and dKO (Fig. 1F). Furthermore, there was no observable difference in the size of the cell bodies of the neurons in the *Rnu11* cKO and dKO compared with the control. The hippocampus was not present in either the *Rnu11* cKO or dKO (Fig. 1F). Further analysis across embryonic development revealed that microcephaly was not discernible at embryonic day (E) 12.5; however, by E14.5 in both the *Rnu11* cKO and dKO microcephaly began precipitating (Fig. S1). Microcephaly in both conditions appears to develop within the same time course, to ultimately present in the severe microcephaly observed at birth (Fig. 1C; Fig. S1).

p53 ablation in *Rnu11* cKO drove the transcriptome towards that of the control

In the *Rnu11* cKO pallium, stabilization of p53 protein resulted in detection of p53 by E12 (Baumgartner et al., 2018). To verify p53 loss in the dKO pallium, we performed immunohistochemistry (IHC) for p53 on E14.5 pallial sections. Although p53 protein was detected in the E14.5 *Rnu11* cKO pallium, we did not observe p53 signal in the dKO (Fig. 2A). As 'intrinsic apoptotic signaling pathway in response to DNA damage by p53 class mediator' was the sole GO term enriched for by the upregulated genes in the E12 *Rnu11* cKO pallium, we explored the impact of p53 ablation on the overall transcriptome (Baumgartner et al., 2018). We have previously shown that cell death in the *Rnu11* cKO pallium begins at E12 and reaches its peak at E14. Therefore, we hypothesized that blocking cell death in the dKO would have the strongest molecular impact at E13.5 and performed bulk Ribo-Zero total RNA-seq of the pallium at E13.5 (n=4 per genotype). Confirmation of clean pallial dissection was determined through RNA-seq analysis of known markers of the region. Expression of *Emx1* and *Lhx2*, another known dorsal telencephalon marker, were high, whereas non-dorsal telencephalon markers from neighboring regions, such as *Dbx1* and *Lhx6*, were not expressed (Table S1) (Grant et al., 2012). Next, we confirmed the genetic manipulation by identifying downregulation of *Rnu11* in the *Rnu11* cKO and downregulation of both *Rnu11* and *Trp53* in the dKO, relative to the control (Table S1). The level of reduction of both *Rnu11* and *Trp53* is commensurate with the number of *Emx1*-Cre negative cells captured in our dissection (Bartolini et al., 2013; Baumgartner et al., 2018).

To interrogate the transcriptome-wide impact of *Trp53* ablation in the *Rnu11* cKO background we performed principal component analysis (PCA) on the three genotypes based on expression of all protein-coding genes. This analysis revealed that the dKO and control transcriptomes were more similar to each other than to that of the *Rnu11* cKO (PC1 48.5%, Fig. 2B). This suggested that activation of p53, a transcription factor, was contributing to the transcriptomic signature of the *Rnu11* cKO, likely driven by the activation of pro-apoptotic pathways. Differential gene expression analysis in the *Rnu11* cKO and control showed a large set of genes that were upregulated in the *Rnu11* cKO (Fig. S2A). However, differential gene expression analysis between the dKO and the control showed that fewer genes were upregulated in the dKO compared with the control (Fig. S2A,B).

Next, we explored the dynamics of gene expression in the *Rnu11* cKO and dKO compared with the control. The intersect analysis allowed us to ask how *Rnu11* ablation alone, compared with dual ablation of *Rnu11* and *Trp53*, affected the transcriptome. For this, we took all protein coding genes that were considered expressed [>1 transcripts per million (TPM) in at least one genotype] and plotted these as an UpSet plot (Fig. 2C). Here, we show that the loss of *Rnu11* resulted in 404 genes being upregulated (OR *Rnu11* cKO), 10,035 non-differentially regulated (NonDR), and three downregulated (OR Control) (Fig. 2C). Within these groups, the majority of MIGs were NonDR in the *Rnu11* cKO (458), whereas only 18 were upregulated and one downregulated (Fig. 2C). In contrast, of the 404 genes upregulated in the *Rnu11* cKO, 274 were

Development (2021) 148, dev199591. doi:10.1242/dev.199591

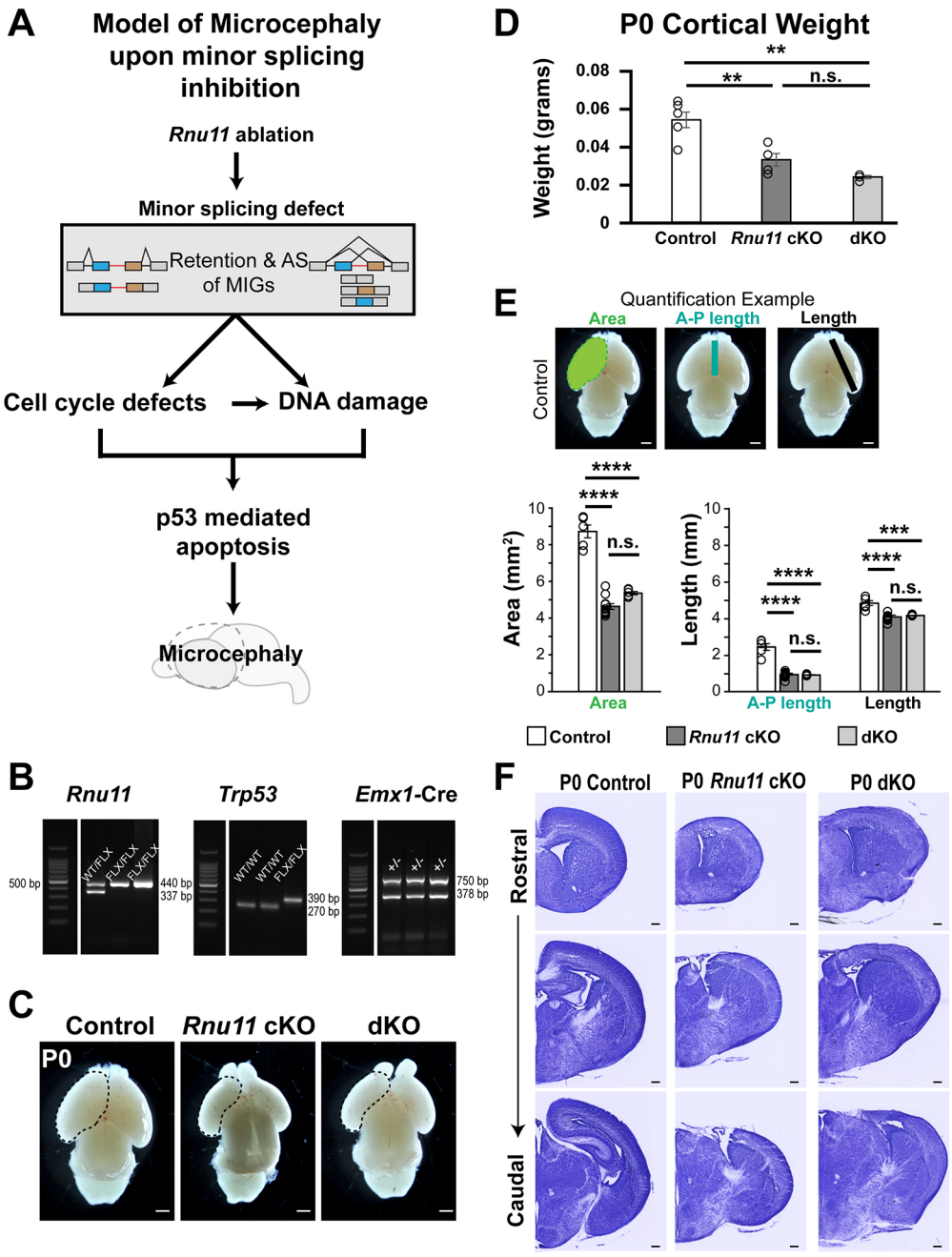

Fig. 1. Removal of *Trp53* in the *Rnu11* cKO mouse does not fully rescue microcephaly. (A) Schematic of the impacts of U11 loss in the *Rnu11* cKO mouse pallium, in which the mis-splicing of MIGs leads to cell cycle defects, DNA damage and p53-mediated cell death, ultimately resulting in microcephaly. Model informed by Baumgartner et al. (2018). (B) Agarose gels for genotype verification of control, *Rnu11* cKO and dKO mice (left to right within each gel) for *Rnu11* (left), *Trp53* (middle) and *Emx1*-Cre (right). Ladder 100 bp MW (Promega). (C) Images of P0 brains of control (left), *Rnu11* cKO (middle) and dKO (right), with left cortices traced in black dotted lines. (D) Bar graph of P0 cortical weights of control (left, white; n=5), *Rnu11* cKO (middle, dark gray; n=4) and dKO (right, light gray; n=3). (E) Top: quantification metrics of hemi-cortical area, anterior-posterior (A-P) length and length. Bottom: bar graphs of hemi-cortical area, A-P length and length for control (white; n=5), *Rnu11* cKO (dark gray; n=10) and dKO (light gray; n=5). (F) Representative brightfield images of Nissl-stained 50 µm thick cryosections of control (left), *Rnu11* cKO (middle) and dKO (right) brains from rostral (top) to caudal (bottom). Data are mean±s.e.m. ****P<0.0001, ***P<0.001, **P<0.01 (one-way ANOVA followed by post-hoc Tukey test). n.s., not significant. Scale bars: 1 mm (C,E); 200 µm (F).

now NonDR upon ablation of *Trp53* in the dKO (Fig. 2C). Most genes (9986) that were NonDR in the *Rnu11* cKO remained NonDR in the dKO (Fig. 2C). However, a subset (29) of genes that were NonDR in the *Rnu11* cKO were downregulated in the dKO (Fig. 2C). It is notable that 12 of these 29 genes were MIGs (Fig. 2C). Finally, of the three downregulated genes in the *Rnu11* cKO, one was a MIG (*Lage3*) that was also downregulated in the dKO. Unlike the three genes downregulated in the *Rnu11* cKO, more genes (32, including 13 MIGs) were downregulated in the dKO (Fig. 2C). The downregulated genes in the dKO enriched for more broad terms including 'nucleosome', 'chromosome', 'chromatin' and 'protein heterodimerization activity', which is consistent with the PCA results (Fig. 2B).

Database for Annotation, Visualization and Integrated Discovery (DAVID) (Huang et al., 2009) analysis of the genes upregulated in the E13.5 *Rnu11* cKO pallium significantly enriched for the GO term 'intrinsic apoptotic pathway through p53 class mediator in response to DNA damage' (Fig. 2D). The genes underpinning this enrichment included *Pmaip1*, *Phlda3*, *Bbc3* and *Aen*, which are downstream targets of p53 in the apoptotic pathway (Fig. 2E). In contrast, similar assessment of the genes upregulated in the dKO compared with the control did not reveal any significant functional enrichments. We hypothesized that the p53 effector genes upregulated in the *Rnu11* cKO would be rescued in the dKO. We plotted Log2 fold change (FC) of *Trp53* and the seven p53-effector genes in both the *Rnu11* cKO and dKO compared with the control (Fig. 2E). Consistent with the idea that p53 function is regulated through protein stabilization and not through transcription, we did not observe *Trp53* upregulation the *Rnu11* cKO. However, in the dKO *Trp53* was predictably downregulated (Fig. 2E). All genes except *Pmaip1* were non-differentially expressed in the dKO when compared with the control (Fig. 2E, red bars; Table S1).

Development (2021) 148, dev199591. doi:10.1242/dev.199591

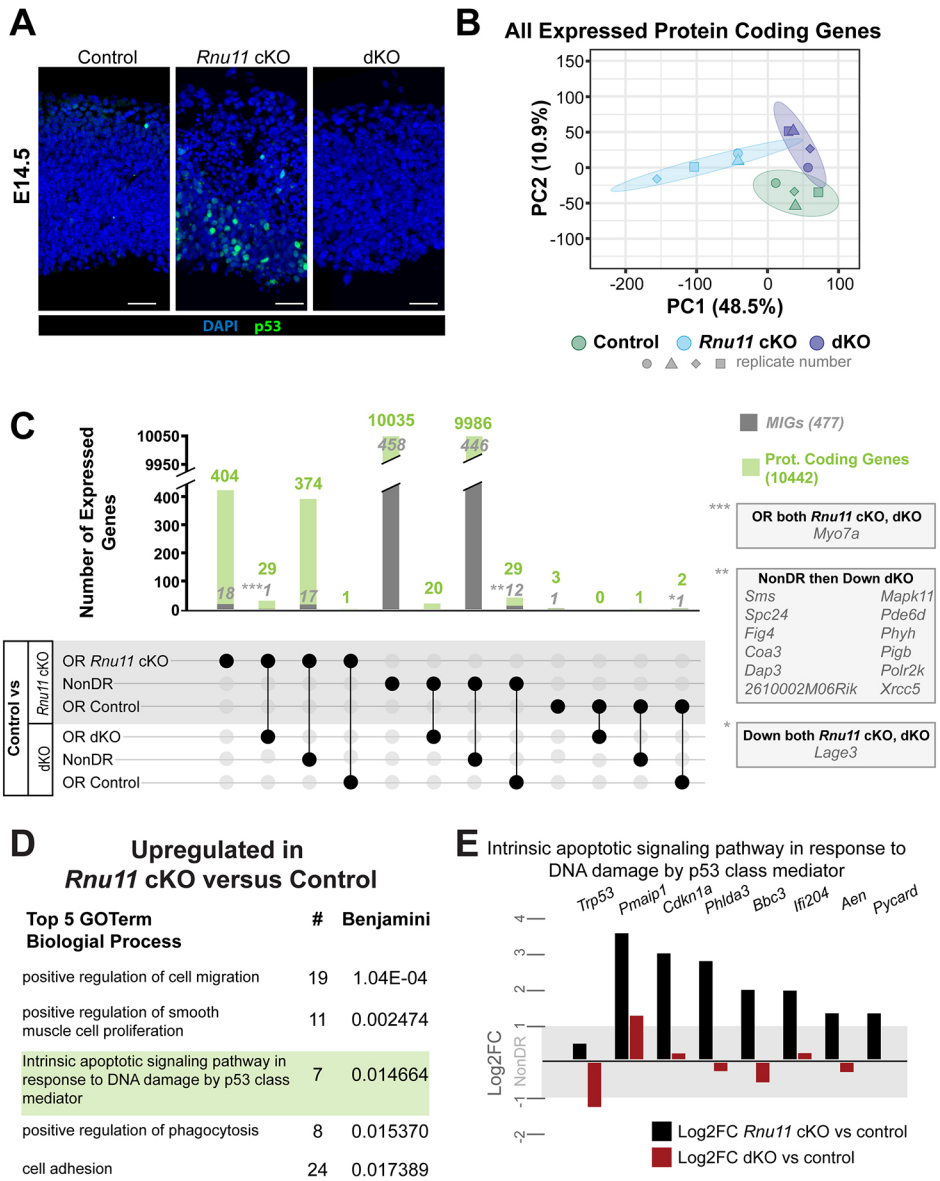

Fig. 2. Removal of p53 rescues the pro-apoptotic molecular phenotype observed in the *Rnu11* cKO pallium. (A) IHC for p53 (green) in E14.5 sagittal sections of the control (left), *Rnu11* cKO (middle) and dKO (right) pallium. Nuclei are marked by DAPI (blue). Scale bars: 20 µm. (B) PCA of all expressed (TPM≥1) protein-coding genes in control (green, *n*=4), *Rnu11* cKO (blue, *n*=4) and dKO (purple, *n*=4). Shapes represent different biological replicates and colored prediction ellipses are drawn such that the probability is 95% that a new observation from the same genotype falls inside the ellipse. (C) UpSet plot representing the intersection of genes that are differentially expressed in the *Rnu11* cKO and dKO compared with the control. The bottom matrix represents the different categories of genes expression, including genes upregulated, downregulated and NonDR in the *Rnu11* cKO and the dKO compared with the control. The black circle represents the category represented in the bar graph above. Two connected black circles represents genes common to those two categories with the bar graph representing the number of genes. Green bars represent all protein-coding genes and gray bars indicate the number of MIGs within that category. Asterisks correspond to boxes on the right listing the specific MIGs within that intersection. (D) Table of top 5 GO terms with significant enrichment by genes upregulated in the E13.5 *Rnu11* cKO compared with the control, identified by DAVID analysis. The term 'intrinsic apoptotic signaling pathway in response to DNA damage by p53 class mediator' is highlighted in green. (E) Bar chart of Log2FC values of the seven genes enriching for the green highlighted GO term in the *Rnu11* cKO versus control comparison (black), and their Log2FC in the dKO versus control comparison (red). The gray horizontal bar indicates the range of non-differential expression (NonDR) calls.

Minor intron splicing defect was not rescued by p53 ablation

The failure of p53 ablation to rescue microcephaly in the *Rnu11* cKO led us to explore whether the expected primary defect, impaired minor intron splicing, was present in the dKO. As anticipated, both the *Rnu11* cKO and dKO displayed significantly elevated minor intron retention, quantified by mis-splicing index (MSI), relative to the control (Fig. 3A; Baumgartner et al., 2018). In contrast, the median MSI of minor introns was not significantly different between the *Rnu11* cKO and dKO (Fig. 3A). Unlike PCA with gene expression, PCA on minor intron retention (%MSI) values revealed clustering of the *Rnu11* cKO and dKO samples away from the control (Fig. 3B). Specifically, we identified 265 and 231 MIGs with significantly increased minor intron retention in the *Rnu11* cKO and dKO compared with the control, respectively (Fig. S3A). There were 210 shared minor intron retention events between the *Rnu11* cKO and the dKO compared with the control (Fig. S3A). DAVID analysis on these 210 MIGs showed enrichment for multiple GO terms, including 'cell cycle', 'cellular response to DNA damage stimulus' and 'mitotic nuclear division' (Fig. S3A). DAVID analysis on the *Rnu11* cKO-specific and dKO-specific MIGs with elevated minor intron retention independently revealed 'mRNA transport' and 'protein transport' for the *Rnu11* cKO-specific MIGs, whereas no GO terms were significantly enriched for the MIGs in the dKO (Fig. S3A).

The retention of minor introns is often predicted to introduce a premature stop codon, resulting in nonsense-mediated decay (NMD), nuclear degradation or the production of aberrant protein (Nagy and Maquat, 1998; Houseley and Tollervey, 2009; Olthof et al., 2021). To further parse the functional impacts of elevated minor intron retention on each MIG, we analyzed the open reading frame (ORF) of all MIGs with significantly elevated minor intron retention in at least one of the two conditions (Baumgartner et al., 2018). Of the 265 MIGs with increased minor intron retention in the *Rnu11* cKO compared with the control, the majority (258/265; 97.4%) of the retained transcripts were predicted to contain a premature stop codon (Fig. 3C). Of those with premature stop codons, 241 were predicted to be targeted for degradation via NMD, whereas 17 of these transcripts were predicted to be translated and produce truncated proteins (Fig. 3C). Similarly, of the 231 MIGs with significantly elevated minor intron retention in the dKO relative to the control, the majority (223/230, 97.0%) were

Development (2021) 148, dev199591. doi:10.1242/dev.199591

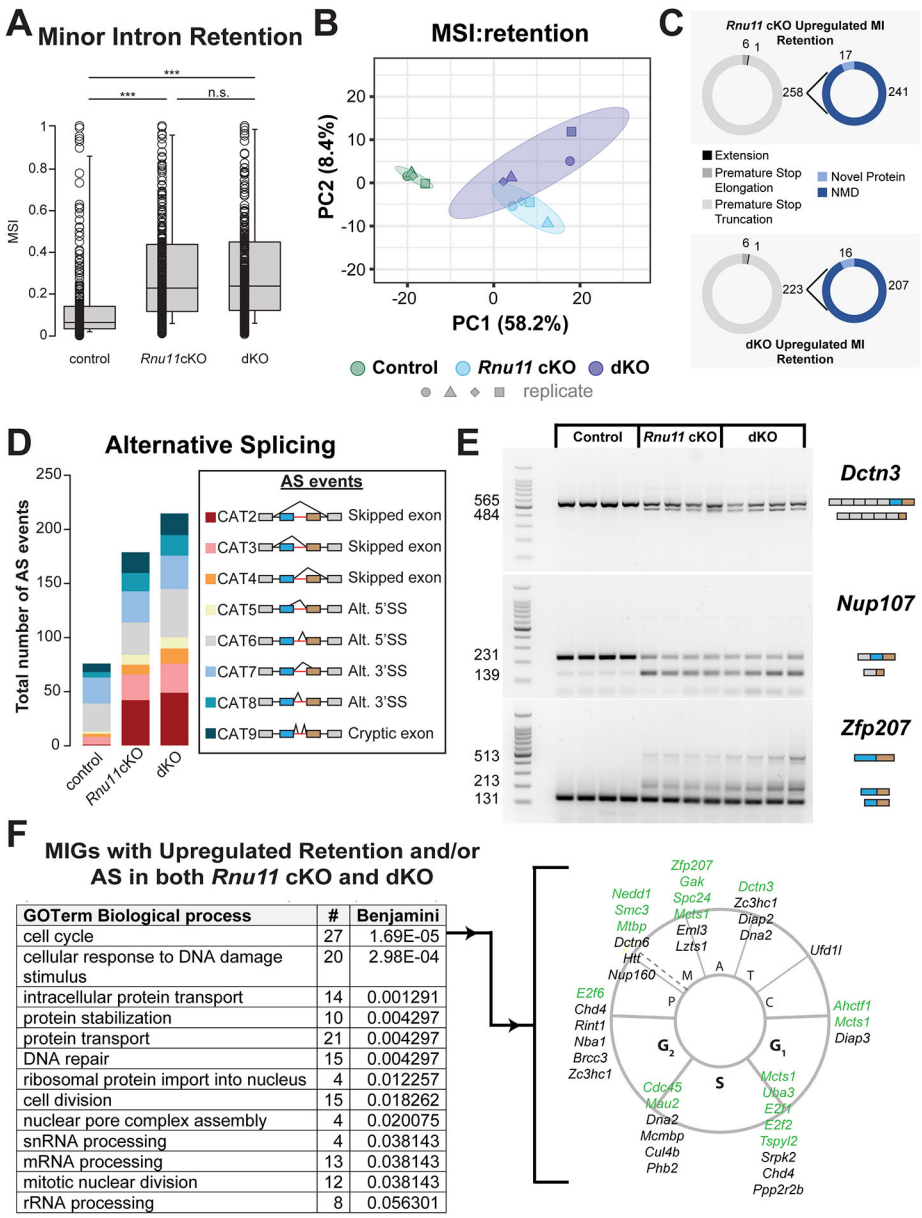

GOTerm Biological process	#	Benjamini
cell cycle	27	1.69E-05
cellular response to DNA damage stimulus	20	2.98E-04
intracellular protein transport	14	0.001291
protein stabilization	10	0.004297
protein transport	21	0.004297
DNA repair	15	0.004297
ribosomal protein import into nucleus	4	0.012257
cell division	15	0.018262
nuclear pore complex assembly	4	0.020075
snRNA processing	4	0.038143
mRNA processing	13	0.038143
mitotic nuclear division	12	0.038143
rRNA processing	8	0.056301

Fig. 3. Primary defect of mis-splicing of minor intron-containing genes involved in cell cycle is comparable in the *Rnu11* cKO and dKO. (A) Boxplot showing the 10th to 90th percentiles of the median MSI for all (*n*=402) minor introns that show retention in any of the three conditions. ***P<0.001 (Kruskal–Wallis H test). n.s., not significant. (B) PCA of minor intron retention (minor intron MSI) in control (blue, *n*=4), *Rnu11* cKO (green, *n*=4) and dKO (purple, *n*=4). Shapes represent different biological replicates and colored prediction ellipses are drawn such that the probability is 95% that a new observation from the same genotype falls inside the ellipse. (C) Left: charts of predicted consequences of minor intron retention on the ORF of MIGs with elevated minor intron retention in the *Rnu11* cKO (top left, grayscale) and the dKO (bottom left, grayscale) relative to control. Right: charts representing whether premature stop codons due to minor intron retention are predicted to trigger NMD or novel protein production in the *Rnu11* cKO (top right, blue) and dKO (bottom right, blue). (D) Bar graph of AS events around minor introns in the control, *Rnu11* cKO and dKO. Schematics of the different types of AS events color-coded in the bar graph are displayed in the key on the right. (E) Agarose gel images of selected AS events around the minor intron of cell cycle-related MIGs as detected by RT-PCR. *n*=4 per genotype. (F) Left: table of Biological Process GO terms enriched by MIGs with shared upregulation of minor intron retention and/or AS in both the *Rnu11* cKO and dKO compared with the control. Right: cell cycle schematic showing MIGs enriching for the top biological process ('cell cycle'; green text), located within the specific cell cycle stage(s)/transition(s) they associate. MIGs listed in black text also regulate cell cycle, do not enrich for the specific GO term and are similarly distributed in the cell cycle schematic.

predicted to introduce a premature stop codon. Of those predicted to contain a premature stop codon, 207 were predicted to be targets for NMD, and the remaining 16 were predicted to result in the production of truncated proteins (Fig. 3C).

The potential targeting of MIG transcripts with minor intron retention by NMD would prevent protein production from these transcripts, thus driving severe repression of the cellular functions performed by these MIGs. To identify these MIG-regulated functions, we performed GO term enrichment analysis using the shared and unique lists of MIGs with significantly elevated minor intron retention predicted to be targets of NMD. Similar to our analysis of all MIGs with elevated minor intron retention, we found that the MIGs with elevated minor intron retention in both the *Rnu11* cKO and dKO significantly enriched for terms including 'cell cycle', 'cell division' and 'cellular response to DNA damage stimulus' (Fig. S3B). As before, the MIGs with unique events in the *Rnu11* cKO and dKO enriched only for 'protein transport' and 'mRNA transport', or had no significant enrichments, respectively (Fig. S3B). This suggested that the underlying minor intron splicing defect and the subsequent molecular defects are shared in the *Rnu11* cKO and dKO.

In addition to minor intron retention, disruption of the minor spliceosome can trigger major spliceosome-mediated AS around minor introns (Olthof et al., 2019, 2021). Using a previously published, minor intron-focused alternative splicing-specific MSI calculation strategy, we identified 76, 179 and 215 AS events in the control, *Rnu11* cKO and dKO, respectively (Olthof et al., 2019). Of these AS events, 119 were upregulated in the *Rnu11* cKO compared with the control, and 156 in the dKO compared with the control (Fig. 3D; Fig. S3C). In both the *Rnu11* cKO and dKO this increase in AS events was primarily driven by exon skipping events (Fig. 3D, CAT2, CAT3, CAT4). Notably, we observed the greatest increase in the skipping of the upstream and downstream exons flanking the minor intron (CAT2), which was detected only once in the control; however, 42 events were detected in the *Rnu11* cKO and 49 in the dKO (Fig. 3D, red). Moreover, there were few AS events, including CAT6 and CAT7, that were already observed at

Development (2021) 148, dev199591. doi:10.1242/dev.199591

high levels in the control (26, 24) and were further increased in both the *Rnu11* cKO (30, 29) and dKO (45, 31).

Of these upregulated events in the *Rnu11* cKO and dKO relative to the control, there were 105 that were shared. This upregulation of AS around the minor intron was confirmed and visualized for select MIGs through reverse transcriptase-PCR (RT-PCR) analysis (Fig. 3E). For example, the canonically spliced transcript of *Dctn3* was detected across all conditions (Fig. 3E, 565 bp); however, an isoform that skips both exons flanking the minor intron was only observed in the *Rnu11* cKO and the dKO samples (Fig. 3E, CAT3, 484 bp) (Olthof et al., 2021). In the case of *Nup107*, an additional isoform (139 bp) was detected alongside the canonically spliced product (231 bp) in the *Rnu11* cKO and dKO (Fig. 3E, CAT3+CAT7). This AS event was the result of skipping of the exon upstream of the minor intron and the use of an alternative 3′ splice site in the exon downstream of the minor intron, which was observed in both the *Rnu11* cKO and dKO (Olthof et al., 2021). Finally, in *Zfp207*, in addition to the presence of the canonical splicing event around the minor intron (131 bp), we validated two AS events around the minor intron, one using alternative 5′ and 3′ splice site (Fig. 3E, CAT6+CAT8, 513 bp) and another with only alternative 5′ splice site usage (CAT6, 213 bp). GO term analysis of the MIGs with shared, upregulated AS events in the *Rnu11* cKO and dKO significantly enriched for terms including ‘nucleus’, ‘kinetochore’ and ‘condensed chromosome kinetochore’ (Fig. S3C).

Next, we combined the lists of MIGs with shared, upregulated AS events around minor introns with the list of shared MIGs displaying elevated minor intron retention in both the *Rnu11* cKO and dKO. This combined list of mis-spliced MIGs was then subjected to DAVID analysis. The most significantly enriched GO term by the shared mis-spliced MIGs was ‘cell cycle’ (Fig. 3F). The mis-spliced MIGs underlying this enrichment were found to be involved in all stages of the cell cycle (Fig. 3F, green text). Notably, we found several mis-spliced MIGs that were missed by DAVID enrichment that had literature support for their involvement in regulating various stages of the cell cycle (Fig. 3F, black text).

Mitotic progression defects in RGCs were exacerbated in the dKO

As the minor splicing defect in the dKO was similar to that of *Rnu11* cKO, we predicted disrupted cell cycle as the primary driver of microcephaly in the dKO. In agreement, functional enrichment analyses of the MIGs with aberrant minor intron splicing revealed mitosis would be particularly affected in the dKO pallium. In our previous report, we found that the RGC population displayed the most significant cell cycle defects, p53 protein upregulation and cell death in the U11-null pallium (Baumgartner et al., 2018). To assess mitosis in RGCs, we performed IHC for the mitotic marker Aurora B and Pax6 to mark RGCs (Gotz et al., 1998), in E12.5, E13.5 and E14.5 pallia from control, *Rnu11* cKO and dKO embryos. For mitotic stage calls, we then used the staining pattern of Aurora B to quantify the percent of mitotic RGCs in each phase of mitosis (Sun et al., 2008; Baumgartner et al., 2018) (Fig. 4; Fig. S4). There was a significant increase in the percentage of mitotic RGCs in prometaphase in both the *Rnu11* cKO and the dKO compared with the control at E12.5, E13.5 and E14.5 (Fig. 4A,B). Concomitantly, there was a reduction in the percentage of RGCs in telophase starting at E13.5 in the dKO that was observed in both the *Rnu11* cKO and dKO at E14.5 (Fig. 4A,B). In addition, there was a significantly lower fraction of mitotic RGCs in metaphase in the dKO when compared with both the *Rnu11* cKO and the control at E12.5 (Fig. S4), which continued in the dKO and was observed in the *Rnu11* cKO at E13.5, and was exacerbated in both conditions at E14.5 (Fig. S4).

Cell cycle length was increased in dKO

The U11-null cells in the *Rnu11* cKO and dKO particularly experience defects in prometaphase-to-metaphase progression (Fig. 4, Fig. S4). However, MIGs involved in S-phase are also mis-spliced in both the *Rnu11* cKO and the dKO pallium (Fig. 3F). As many of the S phase-linked MIGs function in DNA replication, disruption of these MIGs could impact the speed and accuracy of DNA replication. Thus, we sought to interrogate RGCs in S-phase, as well as determine S-phase and total cell cycle length. To do this we pulsed pregnant dams once with BrdU 2 h before harvest, then pulsed once with EdU 30 min before harvest (Fig. 5A) (Martynoga et al., 2005). The percentage of RGCs in S-phase upon harvest was determined by the percentage of Pax6+ RGCs that were also EdU+. At E12.5, the percentage of RGCs in S-phase was comparable across all genotypes (Fig. S5A). However, there was a significant decrease in the percentage of S-phase RGCs in the dKO compared with the control by E13.5. By E14.5, there was a further reduction in the percentage of RGCs in S-phase in both the *Rnu11* cKO and the dKO relative to the control (Fig. S5A). Quantification of the raw number of RGCs across development revealed no significant changes in RGCs across the three genotypes at E12.5 (Fig. S5B). By E13.5, there was a significant reduction in the number of RGCs in the *Rnu11* cKO compared with both the control and dKO, and at E14.5 both the *Rnu11* cKO and dKO had significant reductions in the number of RGCs compared with the control (Fig. S5B).

To interpret these shifts in RGC populations, we calculated their S-phase and the total cell cycle lengths, using both pulses of BrdU and EdU (Fig. 5A). This was followed by IHC for Pax6 and BrdU, coupled with EdU detection. We then used methods described by Martynoga et al. (2005) to calculate the estimated lengths of S-phase and total cell cycle in RGCs. At E12.5, there was a significant increase in the calculated length of S-phase as well as total cell cycle length in the *Rnu11* cKO compared with the control (Fig. 5B, blue fill and black line). By E13.5, the significant increase in S-phase and cell cycle length was no longer observed in the *Rnu11* cKO (Fig. 5B). However, in the dKO there was a significant increase in the total cell cycle length and prolonged G2-G1 length compared with the control (Fig. 5B). Finally, at E14.5, total cell cycle length was significantly increased in the dKO compared with both the control and the *Rnu11* cKO (Fig. 5B). The estimated G2-G1 and total cell cycle lengths in the dKO were too high for them to be physiologically feasible (>30 h), indicating that RGCs most likely had arrested in S-phase in the dKO and, more dramatically, G2-G1 phases (Fig. 5B). Delay in G2-G1 phases was consistent with the significant decrease in the S-phase RGC population at this time-point (Fig. S5A). In contrast, the lengths of S-phase, G2-G1 phases and the total cell cycle in the *Rnu11* cKO were not significantly different from the control at E14.5 (Fig. 5B).

Removal of *Trp53* in *Rnu11* cKO prevented cell death and delayed DNA damage accumulation

Ablation of p53 was performed to block cell death in response to DNA damage and cell cycle defects in the *Rnu11* cKO pallium. Therefore, we next investigated cell death and DNA damage accumulation in the dKO. For this, we performed terminal deoxynucleotidyl transferase dUTP nick-end labeling (TUNEL), a late-stage cell death marker (Kyrylkova et al., 2012), coupled with IHC for cleaved-caspase 3 (CC3) (Faleiro et al., 1997), a marker of early cell death, and γH2AX to detect DNA damage (Sharma et al.,

Development (2021) 148, dev199591. doi:10.1242/dev.199591

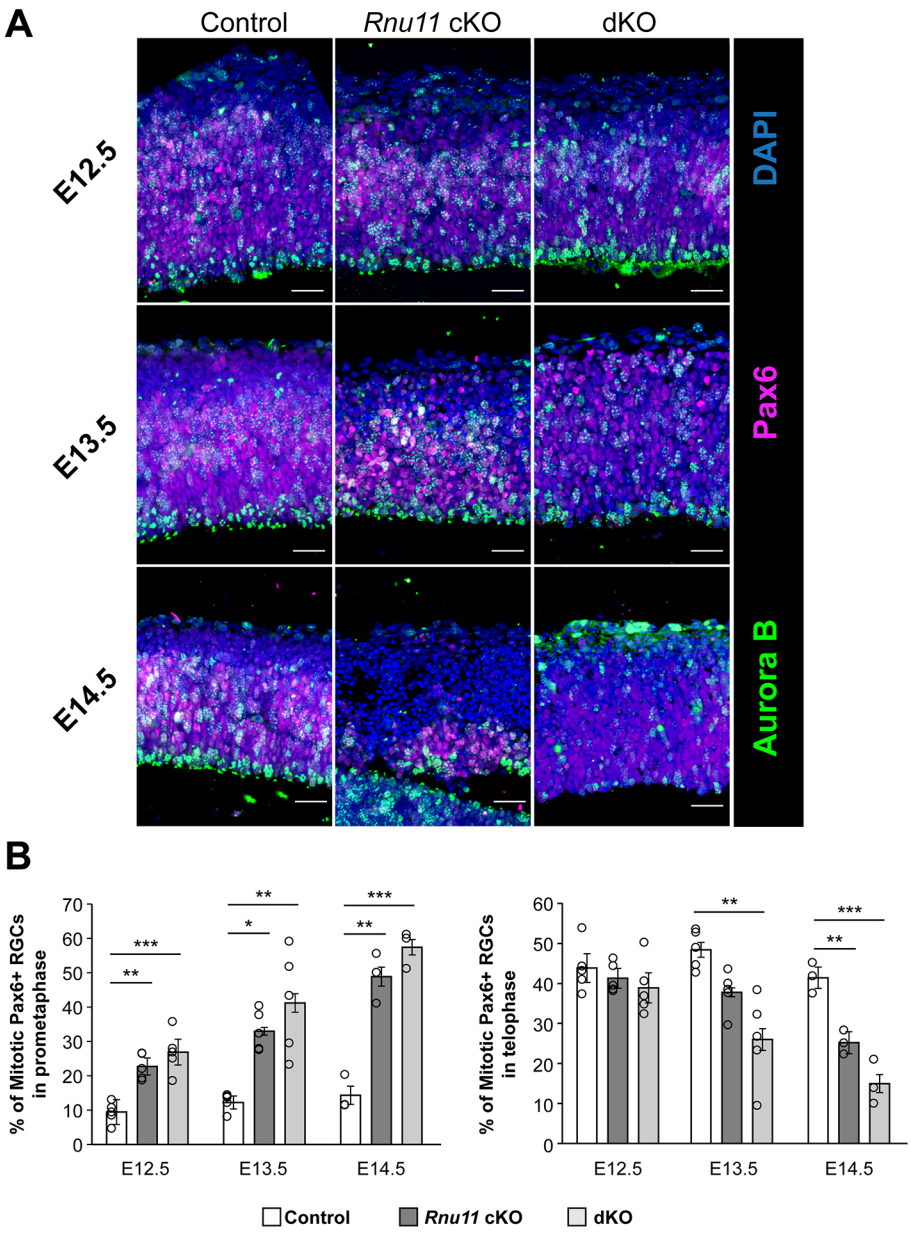

Fig. 4. Mitotic progression of RGCs is significantly impacted in both *Rnu11* cKO and dKO by E12.5. (A) IHC for Aurora B (green) and Pax6 (magenta) on sagittal sections of control (left), *Rnu11* cKO (middle) and dKO (right) pallium across E12.5 (top), E13.5 (middle) and E14.5 (bottom). Nuclei are marked by DAPI (blue). Scale bars: 30 µm. (B) Quantification of the percentage of Aurora B+ mitotic RGCs (Pax6+) across prometaphase (left) and telophase (right) in control, *Rnu11* cKO and dKO across E12.5, E13.5 and E14.5. E12.5 control n=5, *Rnu11* cKO n=5, dKO n=5. E13.5 control n=5, *Rnu11* cKO n=5, dKO n=5. E14.5 control n=3, *Rnu11* cKO n=3, dKO n=3. Data are mean±s.e.m. *P<0.05, **P<0.01, ***P<0.001 (one-way ANOVA, followed by post-hoc Tukey test).

2012). Ablation of p53 successfully blocked cell death, reflected by the absence of TUNEL+ cells or CC3+ cells in the dKO at E12.5, E13.5 and E14.5 compared with the control (Fig. 6A,B). As expected, we observed significant elevation of death, using both markers, in the *Rnu11* cKO compared with both the control and dKO at all time-points (Fig. 6A,B). Unexpectedly, DNA damage, generally thought to drive p53 protein stabilization and p53-mediated apoptosis, was delayed in the dKO, such that significant DNA damage marked by γH2AX was not detected until E14.5 in the dKO compared with the control, which was further increased by E15.5 (Fig. 6A,C; Fig. S6).

DISCUSSION

Unlike mouse models of microcephaly linked to mutations in single genes regulating cell cycle, the microcephaly in *RNU4ATAC*-diseases, including MOPD1, RS and LWS, are linked to the disruption of the minor spliceosome. As the minor spliceosome is responsible for the removal of minor introns found in ∼700 human and mouse genes, perturbations will likely have a broad molecular footprint (Olthof et al., 2019). Thus, the underlying cellular defects that result in microcephaly in such patients proves more difficult to disentangle than most characterized presentations of primary microcephaly. We have previously reported that the *Rnu11* cKO pallium has cell cycle defects and cell death caused by mis-spliced MIGs involved in disparate functions besides the most enriched function of cell cycle regulation (Baumgartner et al., 2018). Importantly, non-MIGs that were upregulated in the *Rnu11* cKO enriched for only one function: intrinsic apoptotic signaling pathway in response to DNA damage by p53 class mediator (Baumgartner et al., 2018). This finding is consistent with those reported in numerous mouse models of microcephaly. Although in most cases blocking cell death through ablation of *Trp53* rescued microcephaly (Insolera et al., 2014; Little and Dwyer, 2019), here we show that ablation of *Trp53* in the *Rnu11* cKO failed to prevent microcephaly (Fig. 1C-F; Fig. S1). This finding suggests that microcephaly in the case of minor spliceosome-related diseases

Development (2021) 148, dev199591. doi:10.1242/dev.199591

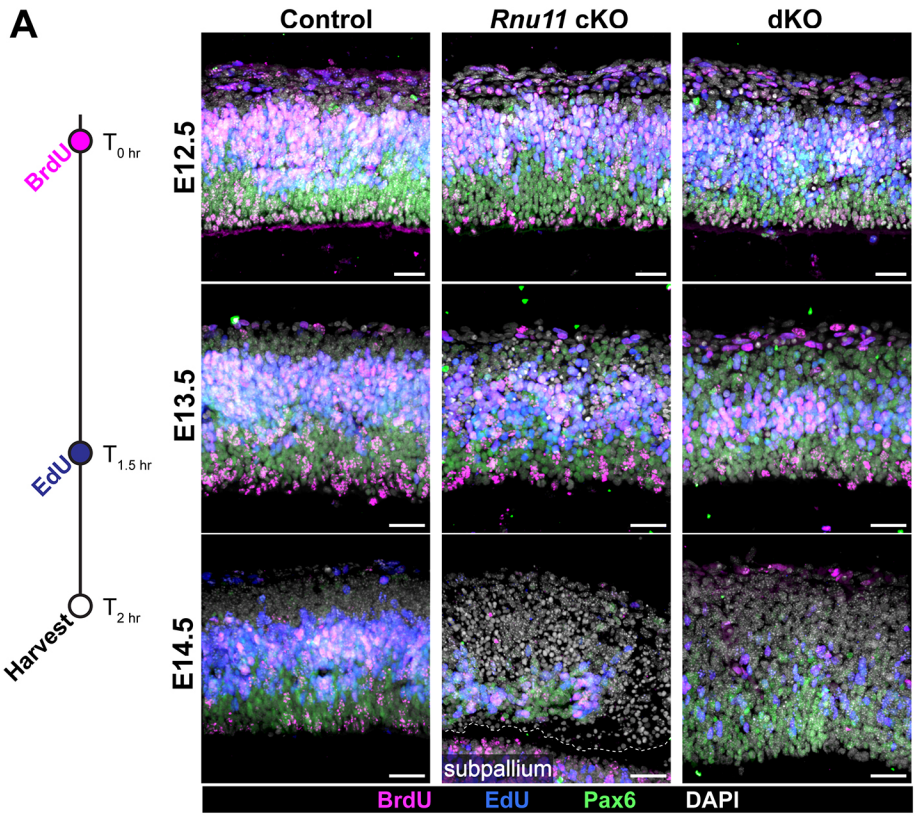

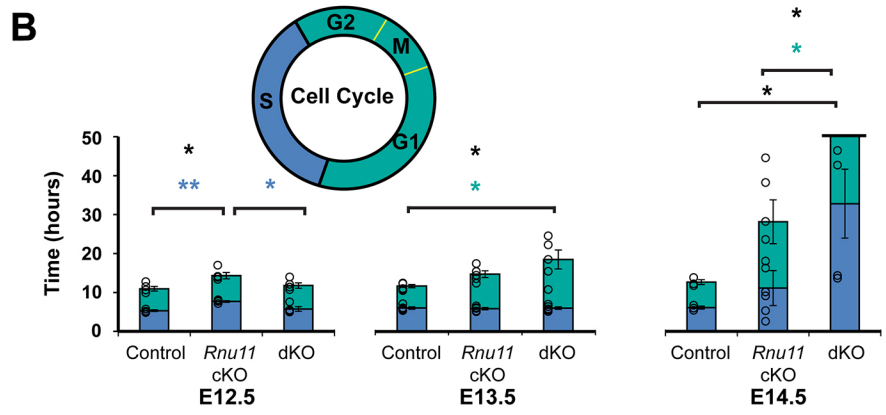

Fig. 5. Total cell cycle length of RGCs is significantly extended in the dKO by E13.5 and E14.5. (A) BrdU/EdU injection paradigm adapted from Martynoga et al. (2005) to quantify total cell cycle speed and S-phase length of RGCs. A single BrdU injection (magenta) was performed at T=0 h, followed by a single EdU injection (blue) at T=1.5 h, with collection at T=2 h (white). Subsequent IHC detection for BrdU and Pax6 (green) was performed in conjunction with EdU detection in sagittal pallial sections of the control (left), *Rnu11* cKO (middle) and dKO (right) at E12.5 (top), E13.5 (middle) and E14.5 (bottom). Nuclei are stained by DAPI (white). Scale bars: 30 µm. (B) Quantification of S-phase (blue), G2-G1 (turquoise) and total cell cycle (full bar, outlined in black) length in the control, *Rnu11* cKO and dKO pallium across E12.5, E13.5 and E14.5, calculated using the method in Martynoga et al. (2005). E12.5 control *n*=4, *Rnu11* cKO *n*=4, dKO *n*=4. E13.5 control *n*=5, *Rnu11* cKO *n*=5, dKO *n*=5. E14.5 control *n*=3, *Rnu11* cKO *n*=5, dKO *n*=4. Data are mean± s.e.m. **P*<0.05, ***P*<0.01 (one-way ANOVA, followed by post-hoc Tukey test). n.s., not significant. Asterisk color indicates the specific comparison tested for statistical significance, corresponding to the bar color-coding scheme.

might not follow the molecular and cellular pathways observed in other diseases. Unlike mutations in single genes that alter cell cycle, which account for the majority of cases of genetically linked primary microcephaly, inhibition of the minor spliceosome affected 178 MIGs via minor intron retention (Baumgartner et al., 2018; Jayaraman et al., 2018). Considering this data, it is not surprising that ablation of *Trp53* did not fully rescue microcephaly in the dKO. The limited rescue we did see is most likely a consequence of the delay in cell death of neural progenitor cells that results in neuron production that is absent in the *Rnu11* cKO mice. Moreover, it is also possible that newly born neurons that might have died in the *Rnu11* cKO might be spared in the dKO where cell death is blocked.

The similarity in the transcriptome profiles of the dKO and control by PCA suggested that transcriptional changes that separated the cKO were driven by p53 activation (Fig. 2B,C; Fig. S2). Thus, the genes downstream of p53 activation such as *Phlda3*, *Bbc3* and *Aen*, which were upregulated in the cKO, were not differentially expressed in the dKO (Fig. 2E). *Pmaip1* was the only gene that was upregulated in the dKO compared with the control; however, based on our filter this gene is considered not expressed in the control and the dKO as it is not expressed above 1 TPM (Fig. 2E; Table S1).

Emx1-Cre progenitor cell heterogeneity in response to minor intron splicing inhibition

The primary microcephaly observed in both the *Rnu11* cKO and dKO resulted not only in reductions in cortex size and length, but also in the complete absence of the hippocampus. Although the primary focus in this paper was the extension of the characterization of the cortical progenitors targeted by *Emx1*-Cre, *Emx1*-Cre also targets the progenitors that give rise to the hippocampus and the inhibitory neurons of the olfactory bulb (Gorski et al., 2002). Given the absence of hippocampal formation in both the *Rnu11* cKO and in the dKO, we anticipate a similar minor intron splicing defect in genes regulating cell cycle (Fig. 1F). Overall, the olfactory bulb morphology appeared unaffected in both the *Rnu11* cKO and the dKO mice (Fig. S1). One possible explanation for this outcome is

Development (2021) 148, dev199591. doi:10.1242/dev.199591

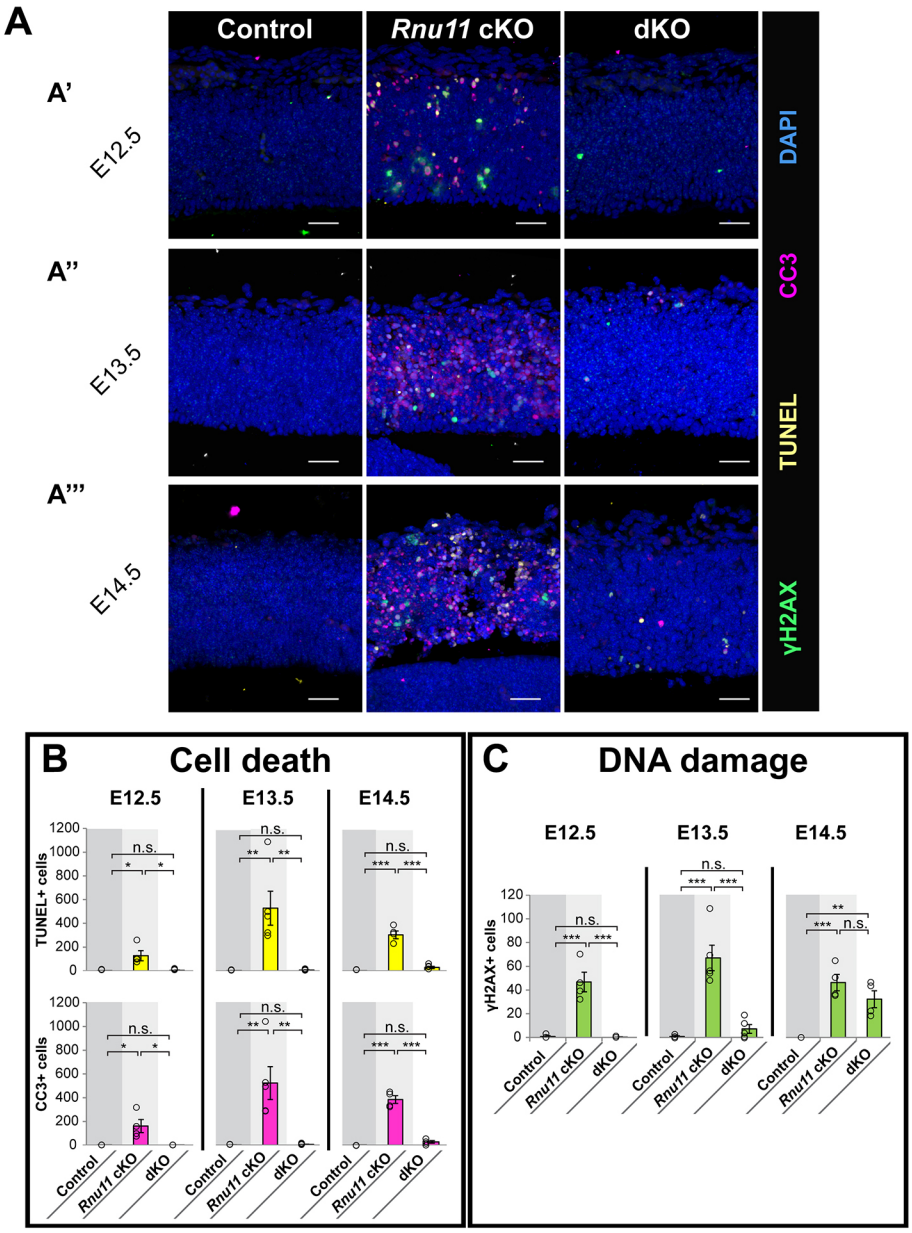

Fig. 6. Removal of p53 in the *Rnu11* cKO inhibits cell death and delays DNA damage. (A) IHC for γH2AX (green), CC3 (magenta) and TUNEL (yellow) on sagittal sections of control (left), *Rnu11* cKO (middle) and dKO (right) pallium across E12.5 (A′), E13.5 (A″) and E14.5 (A‴). Nuclei are marked by DAPI (blue). Scale bars: 30 µm. (B) Quantification of cell death via TUNEL (top) and CC3 (bottom) signal in control, *Rnu11* cKO and dKO pallium across E12.5, E13.5 and E14.5. (C) Quantification of DNA damage via γH2AX signal in control, *Rnu11* cKO and dKO pallium across E12.5, E13.5 and E14.5. E12.5 control n=4, *Rnu11* cKO n=4, dKO n=4. E13.5 control n=5, *Rnu11* cKO n=5, dKO n=5. E14.5 control n=4, *Rnu11* cKO n=4, dKO n=4. Data are mean±s.e.m. *P<0.05, **P<0.01, ***P<0.001 (one-way ANOVA, followed by post-hoc Tukey test). n.s., not significant.

that there are few *Emx1* progenitors that give rise to these inhibitory neurons, thereby reducing the footprint of the observable defect in the olfactory bulb. In all, this finding reflects a progenitor cell heterogeneity of the progenitor cells targeted by *Emx1*-cre, in response to disruptions in minor intron splicing, highlighting that minor intron splicing may play different roles in different developmental pathways.

P53 ablation revealed that disruptions in mitotic progression initiates cell cycle defects upon minor splicing inhibition

We detected cell cycle defects earlier in the dKO compared with the *Rnu11* cKO (Fig. 4A, Fig. S4). One interpretation of this finding is that the RGCs stuck in the cell cycle undergo apoptosis in the *Rnu11* cKO, which is blocked in the dKO (Fig. 6). Surprisingly, at E12.5 we did not observe any significant changes in the percentage of cells in S-phase or in the lengths of S-phase and cell cycle in the dKO (Fig. 5A,B; Fig. S5). This suggests that loss of p53 might ameliorate some of the cell cycle defects, or that this observation was due to the absence of cell death. Consistent with the latter idea, in the *Rnu11* cKO at E13.5 we no longer observed the increase in S-phase and cell cycle length (Fig. 5A,B). However, at this time point, we observed a significant increase in the cell cycle length as well as the length of G2-G1 in the dKO (Fig. 5A,B). Here, one can invoke the idea that the earlier mitotic defects of exaggerated prolongation of prometaphase in the dKO contributes to the calculated increase in G2-G1 length (Fig. 4). Furthermore, at E13.5 we observed no change in the percent of RGCs in S-phase *Rnu11* cKO, which can be explained by accelerated cell death. However, in the dKO at this time point we observed a decrease in the percentage of RGCs in S-phase and thus no change in S-phase length. However, at E14.5 the RGCs stuck in cell cycle are most likely undergoing p53-independent apoptosis at E15.5 (Fig. 5; Fig. S6).

In short, through knocking out *Trp53* in the *Rnu11* cKO we established the temporal kinetics of the cell cycle defects leading to microcephaly upon disruptions in minor splicing. Our previously published works support the hypothesis that upon minor spliceosome

Development (2021) 148, dev199591. doi:10.1242/dev.199591

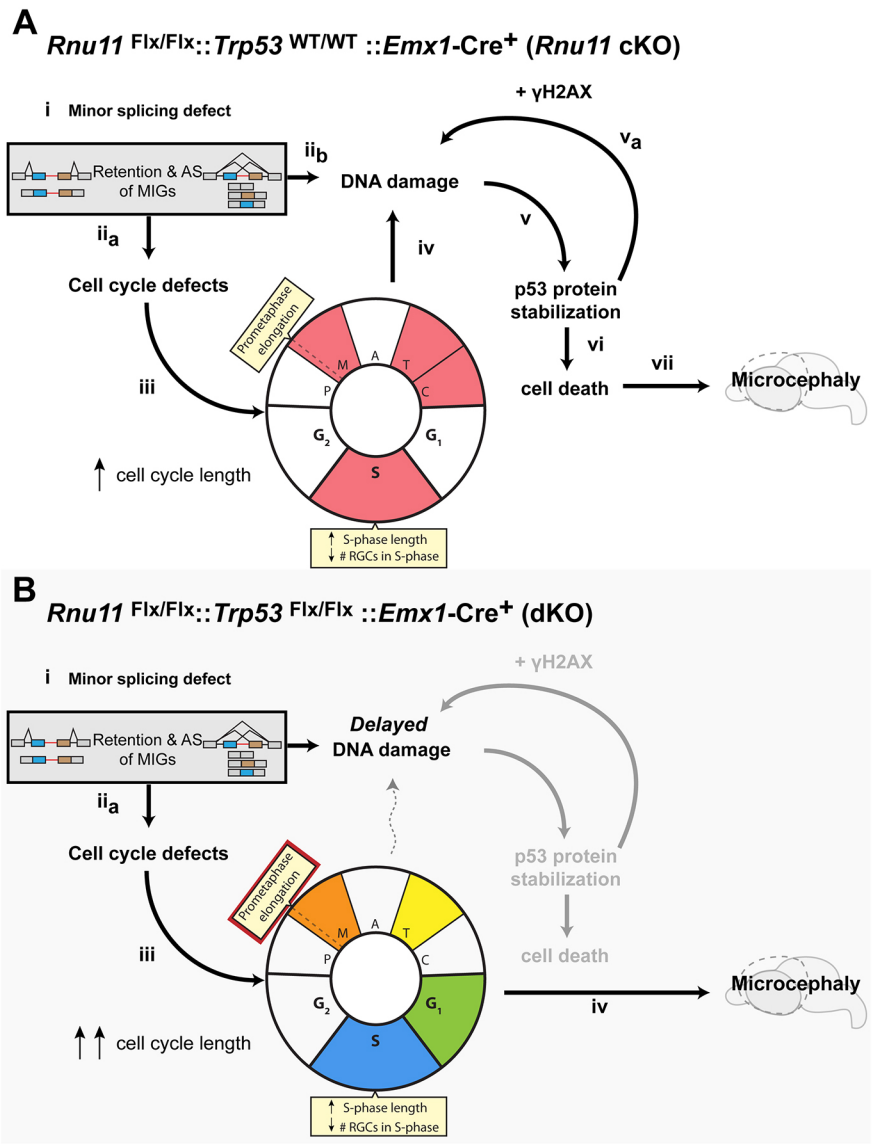

Fig. 7. Model of microcephaly progression upon disruption of the minor spliceosome in the context of p53-mediated cell death. (A) Summary of microcephaly progression upon the disruption of the minor spliceosome in the *Rnu11* cKO, with insights from previous work and this study (Baumgartner et al., 2018; Olthof et al., 2021). (B) Microcephaly progression upon the disruption of the minor spliceosome in the absence of cell death via *Trp53* ablation in the dKO. Grayed out regions indicate nodes rescued upon genetic ablation of *Trp53*. Dashed arrow indicates potential, but unproven, relationship. Color coding of cell cycle defects determines temporal kinetics (red, first to blue, last) of cellular defects that occur as a result of mis-splicing of MIGs.

inhibition, minor splicing defects, including minor intron retention and AS around minor introns, predominantly impact cell cycle-related genes, leading to simultaneous cell cycle defects and DNA damage (Fig. 7Ai,Aii$_a$,Aii$_b$). We observed cell cycle defects including elongation of prometaphase, followed by shortening of metaphase and telophase, a reduction in cytokinetic midbodies and S-phase defects (Fig. 7Aiii). These defects, along with the primary defect of mis-splicing of MIGs involved in DNA damage and repair mechanisms, culminate in DNA damage (Fig. 7Aii$_b$,Aiv). This DNA damage then triggers p53 protein stabilization, which further amplifies DNA damage deposition through γH2AX and leads to cell death (Fig. 7Av,Av$_a$,Avi). Ultimately, the cell cycle defect and cell death of RGCs leads to primary microcephaly in the *Rnu11* cKO mice (Fig. 7Avii).

The current study provides us insight into the more precise temporal kinetics of the cell cycle defects occurring in the *Rnu11* cKO, by blocking cell death. We observed similar primary defects of the mis-splicing of MIGs involved in cell cycle regulation in the dKO (Fig. 7Bi), which results in cell cycle defects, albeit with shifted kinetics (Fig. 7Bii$_a$). In the dKO, p53 ablation exacerbates the mitotic defect. Here, we observed the prometaphase defect a day earlier than in the *Rnu11* cKO, and death at G1 is blocked (Figs 4 and 7Biii, gray node). Instead, these RGCs are stuck in G1 or later phases in the cell cycle (Figs 5 and 7Biii). Furthermore, we observed increased severity in the S-phase defects in the dKO, including decreased number of RGCs in S-phase and a marked increase in the length of S-phase for those RGCs able to progress to this phase of the cell cycle (Figs 4 and 7Biii; Fig. S2). In the dKO we did not observe significant cell death, but by E14.5 and E15.5 we eventually observed significant DNA damage accumulation (Fig. 6C; Fig. S6A,B). Ultimately this suggests that microcephaly caused by disruptions in the minor spliceosome are primarily driven by defects in cell cycle (Fig. 7Biv).

DNA damage, cell death and p53 ablation in the context of disruptions of the minor spliceosome

Ablation of *Trp53* blocked cell death, which most likely allowed us to detect these exaggerated cell cycle defects in the dKO. This is supported by the absence of CC3+ and TUNEL+ cells across E12.5 to E14.5. Surprisingly, we did not observe γH2AX+ cells until E14.5 and E15.5 in the dKO (Fig. 6A,C; Fig. S6). This finding is not consistent with the idea that the accumulation of DNA damage is the

Development (2021) 148, dev199591. doi:10.1242/dev.199591

trigger that activates p53, which results in apoptosis. Thus, p53 might participate in DNA damage in the context of disruption of the minor spliceosome. This idea is supported by evidence in cancer cells where, in a triple knockout (*Rb*, *p107*, *p130*), MEFs in which *Trp53* was ablated showed reduction in DNA damage (Benedict et al., 2018). This suggests that in the *Rnu11* cKO, p53 stabilization in response to DNA damage may feedback to further hasten the accumulating DNA damage; however, in the dKO, the absence of p53 reduces the speed at which DNA damage accumulates. In this study, we reveal that microcephaly due to perturbations in the minor spliceosome is primarily driven by cell cycle defects, while shedding light on the interplay between cell cycle defects, DNA damage, activation of p53 and cell death and its relationship to pathology.

MIGs affected in the U11-null pallium are individually linked to diseases associated with microcephaly

The core set of 244 MIGs mis-spliced in both the *Rnu11* cKO and the dKO enrich for functions including cell cycle and DNA damage response by DAVID analysis (Fig. 3F). This finding suggests that the 244 MIGs underpin microcephaly observed in both *Rnu11* cKO and dKO. Broadly, through generating the *Rnu11* cKO and the dKO mice, we were seeking to understand how perturbations in the minor spliceosome could result in microcephaly pathology. Given that we detected mis-splicing of MIGs in a shared set of MIGs and that we observed primary microcephaly in both conditions, we sought to use this core mis-spliced MIG list to inform pathology. To do this, we investigated whether these MIGs harbored mutations that were linked to microcephaly. Indeed, 19 of the 244 MIGs affected in both the *Rnu11* cKO and the dKO themselves lead to diseases in humans characterized by microcephaly, highlighting that these core mis-spliced MIGs may drive microcephaly progression in minor spliceosome disease (Olthof et al., 2020).

MATERIALS AND METHODS

Animal husbandry

Mouse husbandry and procedures were carried out in accordance with protocols approved by the University of Connecticut Institutional Animal Care and Use Committee, which operates under the guidelines of the US Public Health Service Policy for laboratory animal care. The *Rnu11* cKO mouse (*Mus musculus*) used in this study was generated and described by Baumgartner et al. (2018). *Emx1*-Cre was bred into the *Rnu11* cKO line to target *Rnu11* for removal in the developing forebrain (Gorski et al., 2002). *Trp53*^{tm1Brd} mice were obtained from Jackson Laboratory (JAX stock #008462). For matings intended for embryonic harvests, E0.5 was considered noon the morning a vaginal plug was observed. The experiments described above used male and female *Rnu11*$^{WT/Flx}$::*Trp53*$^{WT/WT}$::*Emx1*-Cre^{+} (control), *Rnu11*$^{Flx/Flx}$::*Trp53*$^{WT/WT}$::*Emx1*-Cre^{+} (*Rnu11* cKO) and *Rnu11*$^{Flx/Flx}$::*Trp53*$^{Flx/Flx}$ ::*Emx1*-Cre^{+} (dKO) embryos.

TUNEL assay

TUNEL was performed on 16 µm sagittal dorsal telencephalon cryosections (E12.5-E14.5) and 16 µm coronal embryonic head cryosections (E15.5) using the *in situ* cell death detection kit, TMR Red (Roche Diagnostics, 12156792910), in accordance with the manufacturer's instructions.

Immunohistochemistry

For IHC, 16 µm sagittal dorsal telencephalon cryosections (E12.5-E14.5) or 16 µm coronal embryonic head cryosections (E15.5) were used as described previously. Primary antibodies were diluted to 1:50 (MoBu-1 clone mouse anti-BrdU, Santa Cruz Biotechnology, sc-51514), 1:100 (mouse anti-Aurora-B/AIM1, BD Biosciences, 611082), 1:200 (mouse anti-γH2AX, MilliporeSigma, 05-636) or 1:300 (rabbit anti-cleaved caspase 3, Cell Signaling Technology, 9665S; rabbit anti-p53, Leica Microsystems, p53-CM5p; rabbit anti-Pax6, MilliporeSigma, ab2237).

Image acquisition and quantification

IHC-processed slides were imaged using a Leica SP2 confocal microscope, using consistent laser intensity, excitation-emission windows, and gain and offset settings across control, *Rnu11* cKO and dKO sections. For each channel, confocal imaging settings were optimized for fluorescence in the control section for each processed slide. Further processing was performed on IMARIS v8.3.1 (Bitplane) and Photoshop CS4 (Adobe Systems). As with the confocal settings, image processing was identical among images of control, *Rnu11* cKO and dKO sections from the same slide. However, for EdU detection experiments performed on E14.5 pallial sections, EdU signal was very low in *Rnu11* cKO and dKO sections, such that confocal settings suitable to the corresponding control did not capture EdU signal in the *Rnu11* cKO and dKO. Therefore, to identify EdU+ cells in the *Rnu11* cKO and dKO pallium, confocal and IMARIS settings were tailored to these genotypes for quantification purposes. Manual quantification was performed in IMARIS as described in Baumgartner et al. (2018).

Cell cycle speed and S-phase speed BrdU, EdU injections

Timed-pregnant dams were injected with BrdU and EdU (100 nmol/g body weight) as described in Martynoga et al., and shown in Fig. 5 (Martynoga et al., 2005). Detection of BrdU was performed through IHC using the MoBu-1 clone mouse anti-BrdU antibody, which does not cross-react with EdU (Santa Cruz Biotechnology, sc-51514; MobU-1; Liboska et al., 2012). Detection of EdU was performed using the Click-iT EdU Cell Proliferation kit with Alexa Fluor 647 dye (Thermo Fisher Scientific, C10340) in accordance with the manufacturer's instructions.

RNA and cDNA preparation

Pallia were dissected from E13.5 control, *Rnu11* cKO and dKO embryos (n=4 per genotype). Tissue for each embryo was placed in separate aliquots of 100 µl TRIzol (Invitrogen, 15596026) and triturated. RNA isolation was then extracted using the DirectZOL RNA MiniPrep kit (Zymo Research, R2050), in accordance with the manufacturer's instructions. For cDNA preparation for RT-PCR experiments, 300 ng of RNA was used for cDNA synthesis as described by Baumgartner et al. (2015). Primers used for alternative splicing in Fig. 3E are listed in Table S2.

RNA-seq

RNA samples were prepared as described above. Library sample preparation and sequencing were executed by the University of Connecticut's Center for Genome Innovation. Specifically, cDNA library preparation was performed using the Illumina TruSeq Stranded Total RNA Library Sample Prep Kit (RS-122-2201) with RiboZero for ribosomal RNA depletion. Sequencing was performed on the Illumina NextSeq 500 platform. Reads were mapped to the mm10 genome (UCSC genome browser) using Hisat2 (Kim et al., 2015). Isoform and gene expression was determined through IsoEM2, to produce expression values in TPM (Mandric et al., 2017); differential gene expression was then determined using IsoDE2, as previously described (Baumgartner et al., 2018). Minor intron retention and ORF analyses were performed as described in Baumgartner et al., 2018, and alternative splicing around the minor intron was calculated and assessed as described in Olthof et al. (2021). DAVID was employed for functional enrichment analysis of gene sets, with a significance cut-off of Benjamini-Hochberg adjusted P-value<0.05 (Huang et al., 2009). The data reported in this publication have been deposited in NCBI's Gene Expression Omnibus and are accessible through GEO Series accession number GSE168366.

Principal component analysis

PCA was performed based on protein coding gene expression (TPM values), retention levels (%MSI$_{Ret}$) using the default settings in ClustVis (Metsalu and Vilo, 2015).

Nissl staining

Postnatal day (P) 0 brains were cryosectioned (50 µm) and collected on 1% gelatin and chrome alum-coated glass slides at 200 µm (control) or 150 µm (*Rnu11* cKO and dKO) intervals. Slides were rinsed in distilled water for 1 min, followed by a sequence of ethanol (EtOH) dehydration steps for

2 min each (50% EtOH, 70% EtOH, 95% EtOH, 100% EtOH, 100% EtOH, 100% EtOH). This was followed by two 2-min toluene washes, and then by a sequence of dehydration steps in ethanol, each lasting 2 min (100% EtOH, 100% EtOH, 100% EtOH, 100% EtOH, 95% EtOH, 70% EtOH, 50% EtOH). Slides were rinsed in distilled water for 2 min, followed by 3 min in Cresyl Violet (1% cresyl violet+0.25% glacial acetic acid) and another 2 min water rinse. The first dehydration series was repeated, followed by three toluene washes (2 min, 1 min and 1 min). Slides were mounted with Permount mounting medium (Fisher Scientific, SP15-100) and allowed to harden in the fume hood overnight before being imaged and stitched with Keyence BZ-X710 at 4×.

P0 cortical parameter quantifications

P0 brains were dissected and imaged from the top-view under white light in the dissecting scope. The hemi-cortical surface area, anterior-posterior length and cortical length were measured by ImageJ on the images of freshly harvested P0 brains as reported in Ka et al. (2021).

Statistical methods

All statistical tests and results used in this article are outlined in Table S3.

Acknowledgements

We thank Dr Bo Reese from the University of Connecticut's Center for Genome Innovation for assistance with RNA-seq; Dr Ion Mandoiu from the University of Connecticut's Computer Science and Engineering Department for the establishment and maintenance of bioinformatics platforms.

Competing interests

The authors declare no competing or financial interests.

Author contributions

Conceptualization: R.N.K.; Methodology: A.K.W., M.B., K.D.D., G.S.A., R.N.K.; Validation: A.K.W., M.B., M.F.L., G.S.A.; Investigation: A.K.W., M.B., M.F.L., G.S.A., R.N.K.; Resources: R.N.K.; Data curation: A.K.W., M.B., M.F.L.; Writing - original draft: A.K.W., M.B., R.N.K.; Writing - review & editing: A.K.W., R.N.K.; Visualization: A.K.W., M.B., K.D.D., R.N.K.; Supervision: R.N.K.; Funding acquisition: R.N.K.

Funding

Funding for this study comes from National Institutes of Health/National Institute of Neurological Disorders and Stroke (R01NS102538). Deposited in PMC for release after 12 months.

Data availability

RNA-seq data have been deposited in GEO under accession number GSE168366.

Peer review history

The peer review history is available online at https://journals.biologists.com/dev/article-lookup/doi/10.1242/dev.199591

References

Bartolini, G., Ciceri, G. and Marín, O. (2013). Integration of GABAergic interneurons into cortical cell assemblies: lessons from embryos and adults. *Neuron* **79**, 849-864. doi:10.1016/j.neuron.2013.08.014

Baumgartner, M., Lemoine, C., Al Seesi, S., Karunakaran, D. K. P., Sturrock, N., Banday, A. R., Kilcollins, A. M., Mandoiu, I. and Kanadia, R. N. (2015). Minor splicing snRNAs are enriched in the developing mouse CNS and are crucial for survival of differentiating retinal neurons. *Dev. Neurobiol.* **75**, 895-907. doi:10.1002/dneu.22257

Baumgartner, M., Olthof, A. M., Aquino, G. S., Hyatt, K. C., Lemoine, C., Drake, K., Sturrock, N., Nguyen, N., Al Seesi, S. and Kanadia, R. N. (2018). Minor spliceosome inactivation causes microcephaly, owing to cell cycle defects and death of self-amplifying radial glial cells. *Development* **145**, dev166322. doi:10.1242/dev.166322

Baumgartner, M., Drake, K. and Kanadia, R. N. (2019). An integrated model of minor intron emergence and conservation. *Front. Genet.* **10**, 1113. doi:10.3389/fgene.2019.01113

Bazzi, H. and Anderson, K. V. (2014). Acentriolar mitosis activates a p53-dependent apoptosis pathway in the mouse embryo. *Proc. Natl. Acad. Sci. USA* **111**, E1491-E1500. doi:10.1073/pnas.1400568111

Benedict, B., van Harn, T., Dekker, M., Hermsen, S., Kucukosmanoglu, A., Pieters, W., Delzenne-Goette, E., Dorsman, J. C., Petermann, E., Foijer, F. et al. (2018). Loss of p53 suppresses replication-stress-induced DNA breakage in G1/S checkpoint deficient cells. *eLife* **7**, e37868. doi:10.7554/eLife.37868

Burge, C. B., Padgett, R. A. and Sharp, P. A. (1998). Evolutionary fates and origins of U12-type introns. *Mol. Cell* **2**, 773-785. doi:10.1016/S1097-2765(00)80292-0

Chen, W. J., Maier, S. E., Parnell, S. E. and West, J. R. (2003). Alcohol and the developing brain: neuroanatomical studies. *Alcohol Res. Health* **27**, 174-180.

Cheng, Q. and Chen, J. (2010). Mechanism of p53 stabilization by ATM after DNA damage. *Cell Cycle* **9**, 472-478. doi:10.4161/cc.9.3.10556

Dehay, C. and Kennedy, H. (2007). Cell-cycle control and cortical development. *Nat. Rev. Neurosci.* **8**, 438-450. doi:10.1038/nrn2097

Douglas, R. J., Koch, C., Mahowald, M., Martin, K. A. C. and Suarez, H. H. (1995). Recurrent excitation in neocortical circuits. *Science* **269**, 981-985. doi:10.1126/science.7638624

Edery, P., Marcaillou, C., Sahbatou, M., Labalme, A., Chastang, J., Touraine, R., Tubacher, E., Senni, F., Bober, M. B., Nampoothiri, S. et al. (2011). Association of TALS developmental disorder with defect in minor splicing component U4atac snRNA. *Science* **332**, 240-243. doi:10.1126/science.1202205

Faleiro, L., Kobayashi, R., Fearnhead, H. and Lazebnik, Y. (1997). Multiple species of CPP32 and Mch2 are the major active caspases present in apoptotic cells. *EMBO J.* **16**, 2271-2281. doi:10.1093/emboj/16.9.2271

Farach, L. S., Little, M. E., Duker, A. L., Logan, C. V., Jackson, A., Hecht, J. T. and Bober, M. (2018). The expanding phenotype of RNU4ATAC pathogenic variants to lowry wood syndrome. *Am. J. Med. Genet. A* **176**, 465-469. doi:10.1002/ajmg.a.38581

Feldman, H. S., Jones, K. L., Lindsay, S., Slymen, D., Klonoff-Cohen, H., Kao, K., Rao, S. and Chambers, C. (2012). Prenatal alcohol exposure patterns and alcohol-related birth defects and growth deficiencies: a prospective study. *Alcohol Clin. Exp. Res.* **36**, 670-676. doi:10.1111/j.1530-0277.2011.01664.x

Gorski, J. A., Talley, T., Qiu, M., Puelles, L., Rubenstein, J. L. R. and Jones, K. R. (2002). Cortical excitatory neurons and glia, but not GABAergic neurons, are produced in the Emx1-expressing lineage. *J. Neurosci.* **22**, 6309-6314. doi:10.1523/JNEUROSCI.22-15-06309.2002

Götz, M., Stoykova, A. and Gruss, P. (1998). Pax6 controls radial glia differentiation in the cerebral cortex. *Neuron* **21**, 1031-1044. doi:10.1016/S0896-6273(00)80621-2

Grant, E., Hoerder-Suabedissen, A. and Molnár, Z. (2012). Development of the corticothalamic projections. *Front. Neurosci.* **6**, 53. doi:10.3389/fnins.2012.00053

He, H., Liyanarachchi, S., Akagi, K., Nagy, R., Li, J., Dietrich, R. C., Li, W., Sebastian, N., Wen, B., Xin, B. et al. (2011). Mutations in U4atac snRNA, a component of the minor spliceosome, in the developmental disorder MOPD I. *Science* **332**, 238-240. doi:10.1126/science.1200587

Houseley, J. and Tollervey, D. (2009). The many pathways of RNA degradation. *Cell* **136**, 763-776. doi:10.1016/j.cell.2009.01.019

Huang, D. W., Sherman, B. T. and Lempicki, R. A. (2009). Systematic and integrative analysis of large gene lists using DAVID bioinformatics resources. *Nat. Protoc.* **4**, 44-57. doi:10.1038/nprot.2008.211

Insolera, R., Bazzi, H., Shao, W., Anderson, K. V. and Shi, S.-H. (2014). Cortical neurogenesis in the absence of centrioles. *Nat. Neurosci.* **17**, 1528-1535. doi:10.1038/nn.3831

Janisch, K. M., Vock, V. M., Fleming, M. S., Shrestha, A., Grimsley-Myers, C. M., Rasoul, B. A., Neale, S. A., Cupp, T. D., Kinchen, J. M., Liem, K. F.Jr. et al. (2013). The vertebrate-specific Kinesin-6, Kif20b, is required for normal cytokinesis of polarized cortical stem cells and cerebral cortex size. *Development* **140**, 4672-4682. doi:10.1242/dev.093286

Jayaraman, D., Bae, B.-I. and Walsh, C. A. (2018). The genetics of primary microcephaly. *Annu. Rev. Genomics Hum. Genet.* **19**, 177-200. doi:10.1146/annurev-genom-083117-021441

Ka, M., Moffat, J. J. and Kim, W.-Y. (2021). MACF1, involved in the 1p34.2p34.3 microdeletion syndrome, is essential in cortical progenitor polarity and brain integrity. *Cell. Mol. Neurobiol.* [Epub ahead of print]. doi:10.1007/s10571-021-01088-1

Kim, D., Langmead, B. and Salzberg, S. L. (2015). HISAT: a fast spliced aligner with low memory requirements. *Nat. Methods* **12**, 357-360. doi:10.1038/nmeth.3317

Kyrylkova, K., Kyryachenko, S., Leid, M. and Kioussi, C. (2012). Detection of apoptosis by TUNEL assay. *Methods Mol. Biol.* **887**, 41-47. doi:10.1007/978-1-61779-860-3_5

Lakin, N. D. and Jackson, S. P. (1999). Regulation of p53 in response to DNA damage. *Oncogene* **18**, 7644-7655. doi:10.1038/sj.onc.1203015

Levine, A. and Durbin, R. (2001). A computational scan for U12-dependent introns in the human genome sequence. *Nucleic Acids Res.* **29**, 4006-4013. doi:10.1093/nar/29.19.4006

Liboska, R., Ligasová, A., Strunin, D., Rosenberg, I. and Koberna, K. (2012). Most anti-BrdU antibodies react with 2'-deoxy-5-ethynyluridine — the method for the effective suppression of this cross-reactivity. *PLoS ONE* **7**, e51679. doi:10.1371/journal.pone.0051679

Little, J. N. and Dwyer, N. D. (2019). p53 deletion rescues lethal microcephaly in a mouse model with neural stem cell abscission defects. *Hum. Mol. Genet.* **28**, 434-447. doi:10.1093/hmg/ddy350

Mandric, I., Temate-Tiagueu, Y., Shcheglova, T., Al Seesi, S., Zelikovsky, A. and Măndoiu, I. I. (2017). Fast bootstrapping-based estimation of confidence

intervals of expression levels and differential expression from RNA-Seq data. *Bioinformatics* **33**, 3302-3304. doi:10.1093/bioinformatics/btx365

Mao, H., McMahon, J. J., Tsai, Y.-H., Wang, Z. and Silver, D. L. (2016). Haploinsufficiency for core exon junction complex components disrupts embryonic neurogenesis and causes p53-mediated microcephaly. *PLoS Genet.* **12**, e1006282. doi:10.1371/journal.pgen.1006282

Martynoga, B., Morrison, H., Price, D. J. and Mason, J. O. (2005). Foxg1 is required for specification of ventral telencephalon and region-specific regulation of dorsal telencephalic precursor proliferation and apoptosis. *Dev. Biol.* **283**, 113-127. doi:10.1016/j.ydbio.2005.04.005

Merico, D., Roifman, M., Braunschweig, U., Yuen, R. K. C., Alexandrova, R., Bates, A., Reid, B., Nalpathamkalam, T., Wang, Z., Thiruvahindrapuram, B. et al. (2015). Compound heterozygous mutations in the noncoding RNU4ATAC cause roifman syndrome by disrupting minor intron splicing. *Nat. Commun.* **6**, 8718. doi:10.1038/ncomms9718

Metsalu, T. and Vilo, J. (2015). ClustVis: a web tool for visualizing clustering of multivariate data using principal component analysis and heatmap. *Nucleic Acids Res.* **43**, W566-W570. doi:10.1093/nar/gkv468

Nagy, E. and Maquat, L. E. (1998). A rule for termination-codon position within intron-containing genes: when nonsense affects RNA abundance. *Trends Biochem. Sci.* **23**, 198-199. doi:10.1016/S0968-0004(98)01208-0

Olthof, A. M., Hyatt, K. C. and Kanadia, R. N. (2019). Minor intron splicing revisited: identification of new minor intron-containing genes and tissue-dependent retention and alternative splicing of minor introns. *BMC Genomics* **20**, 686. doi:10.1186/s12864-019-6046-x

Olthof, A. M., Rasmussen, J. S., Campeau, P. M. and Kanadia, R. N. (2020). Disrupted minor intron splicing is prevalent in Mendelian disorders. *Mol. Genet. Genomic Med.* **8**, e1374. doi:10.1002/mgg3.1374

Olthof, A. M., White, A. K., Mieruszynski, S., Doggett, K., Lee, M. F., Chakroun, A., Abdel Aleem, A. K., Rousseau, J., Magnani, C., Roifman, C. M. et al. (2021). Disruption of exon-bridging interactions between the minor and major spliceosomes results in alternative splicing around minor introns. *Nucleic Acids Res.* **49**, 3524-3545. doi:10.1093/nar/gkab118

Patel, A. A. and Steitz, J. A. (2003). Splicing double: insights from the second spliceosome. *Nat. Rev. Mol. Cell Biol.* **4**, 960-970. doi:10.1038/nrm1259

Rasmussen, S. A., Jamieson, D. J., Honein, M. A. and Petersen, L. R. (2016). Zika virus and birth defects — reviewing the evidence for causality. *N. Engl. J. Med.* **374**, 1981-1987. doi:10.1056/NEJMsr1604338

Sharma, A., Singh, K. and Almasan, A. (2012). Histone H2AX phosphorylation: a marker for DNA damage. *Methods Mol. Biol.* **920**, 613-626. doi:10.1007/978-1-61779-998-3_40

Silver, D. L., Watkins-Chow, D. E., Schreck, K. C., Pierfelice, T. J., Larson, D. M., Burnetti, A. J., Liaw, H.-J., Myung, K., Walsh, C. A., Gaiano, N. et al. (2010). The exon junction complex component Magoh controls brain size by regulating neural stem cell division. *Nat. Neurosci.* **13**, 551-558. doi:10.1038/nn.2527

Sun, L., Gao, J., Dong, X., Liu, M., Li, D., Shi, X., Dong, J.-T., Lu, X., Liu, C. and Zhou, J. (2008). EB1 promotes Aurora-B kinase activity through blocking its inactivation by protein phosphatase 2A. *Proc. Natl. Acad. Sci. USA* **105**, 7153-7158. doi:10.1073/pnas.0710018105

von der Hagen, M., Pivarcsi, M., Liebe, J., von Bernuth, H., Didonato, N., Hennermann, J. B., Bührer, C., Wieczorek, D. and Kaindl, A. M. (2014). Diagnostic approach to microcephaly in childhood: a two-center study and review of the literature. *Dev. Med. Child Neurol.* **56**, 732-741. doi:10.1111/dmcn.12425

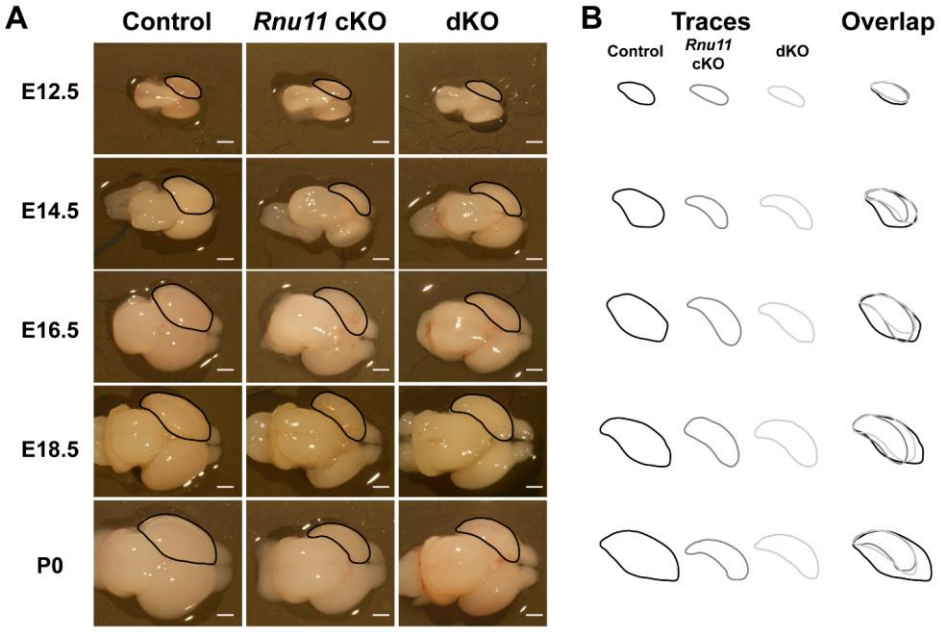

Fig. S1. Developmental timecourse of microcephaly progression in the *Rnu11* cKO and dKO. (A) Representative top-view light images of dissected brains of control (left), *Rnu11* cKO (middle), and dKO (right) at E12.5, E14.5, E16.5, E18.5, and P0. **(B)** Individual traces of left hemisphere of developing cortex at each timepoint in the left 3 columns, with the overlap of traces from each genotype shown in the rightmost column. Scale bar 1mm.

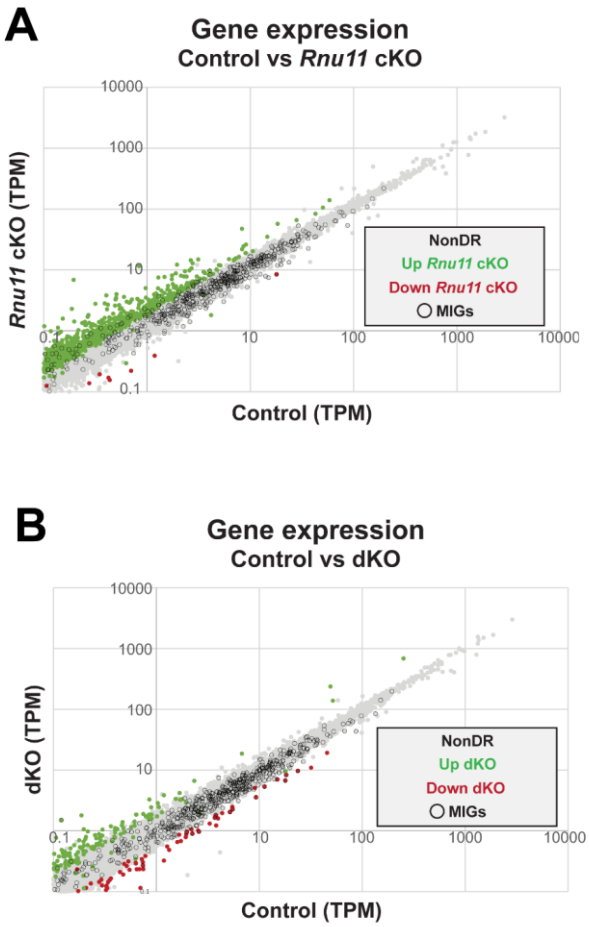

Fig. S2. Comparison of gene expression changes occurring in the *Rnu11* cKO and dKO relative to the control. (A) Scatterplot of gene expression (TPM) of protein-coding genes in the control (x-axis) and *Rnu11* cKO (y-axis) in the E13.5 pallium. Genes non-differentially regulated (NonDR) in grey, upregulated in the *Rnu11* cKO in green, downregulated in the *Rnu11* cKO in red, and MIGs outlined with black circles. **(B)** Scatterplot of gene expression (TPM) of protein-coding genes in the control (x-axis) and dKO (y-axis) in E13.5 pallium. Genes non-differentially regulated (NonDR) in grey, upregulated in the dKO in green, downregulated in the dKO in red, and MIGs outlined with black circles.

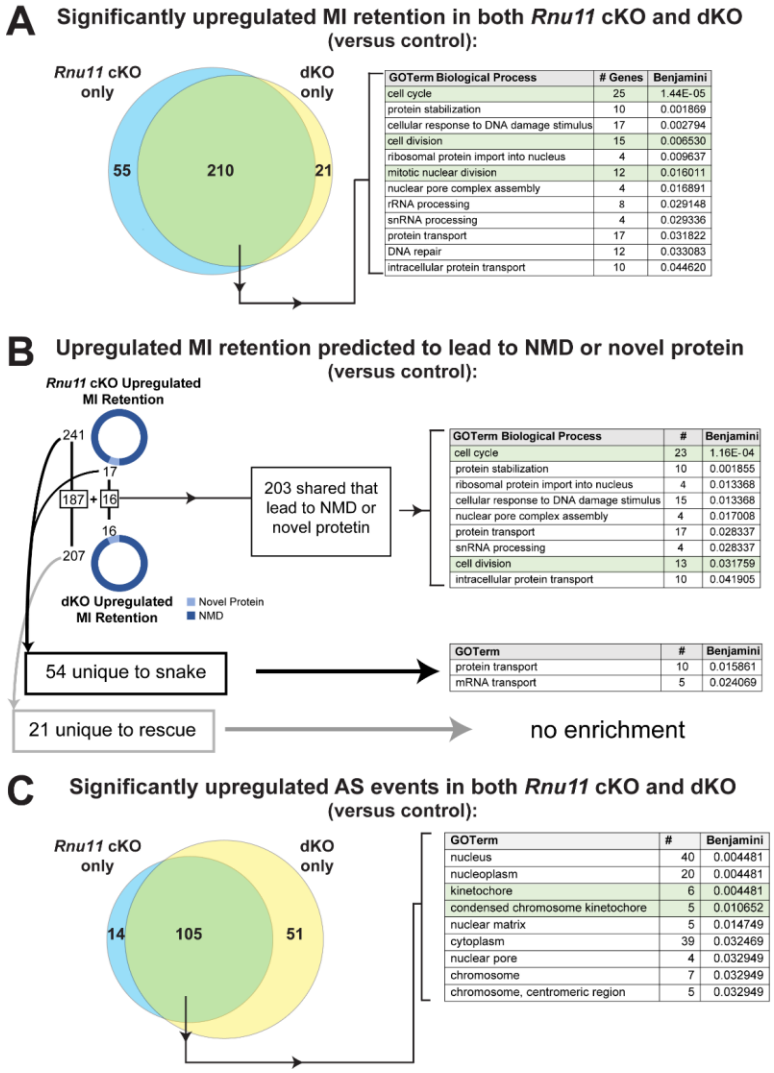

GOTerm Biological Process	# Genes	Benjamini
cell cycle	25	1.44E-05
protein stabilization	10	0.001869
cellular response to DNA damage stimulus	17	0.002794
cell division	15	0.006530
ribosomal protein import into nucleus	4	0.009637
mitotic nuclear division	12	0.016011
nuclear pore complex assembly	4	0.016891
rRNA processing	8	0.029148
snRNA processing	4	0.029336
protein transport	17	0.031822
DNA repair	12	0.033083
intracellular protein transport	10	0.044620

GOTerm Biological Process	#	Benjamini
cell cycle	23	1.16E-04
protein stabilization	10	0.001855
ribosomal protein import into nucleus	4	0.013368
cellular response to DNA damage stimulus	15	0.013368
nuclear pore complex assembly	4	0.017008
protein transport	17	0.028337
snRNA processing	4	0.028337
cell division	13	0.031759
intracellular protein transport	10	0.041905

GOTerm	#	Benjamini
protein transport	10	0.015861
mRNA transport	5	0.024069

GOTerm	#	Benjamini
nucleus	40	0.004481
nucleoplasm	20	0.004481
kinetochore	6	0.004481
condensed chromosome kinetochore	5	0.010652
nuclear matrix	5	0.014749
cytoplasm	39	0.032469
nuclear pore	4	0.032949
chromosome	7	0.032949
chromosome, centromeric region	5	0.032949

Fig. S3. Comparison of primary minor splicing defects in the Rnu11 cKO and dKO. (A) Venn-Diagram of the number of MIGs with significantly elevated retention in the Rnu11 cKO (blue) and dKO (yellow) compared to the control (left). Table of Biological Process GO Term enrichment of the shared minor intron retention with cell cycle highlighted in green (right). (B) Comparison of the minor intron retention even predicted to lead to disrupt the open reading frame (ORF), thus predicted to be targeted for nonsense mediated decay (NMD). Of the 203 shared events predicted to be targeted for NMD between the *Rnu11* cKO and dKO, Biological Process GO Term enrichment, with cell cycle highlighted in green (right). Unique events in the *Rnu11* cKO enriched for protein and mRNA transport. Unique events in the dKO revealed no significant enrichment. **(C)** Venn-Diagram of the number of significantly upregulated alternative splicing events around minor introns in the *Rnu11* cKO (blue) and dKO (yellow) compared to the control (left). Table of GO Term enrichment of the shared AS with cell cycle-related highlighted in green (right).

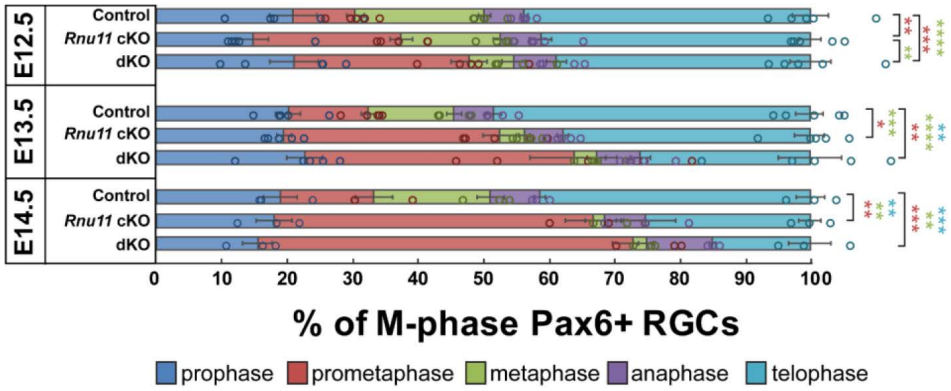

Fig. S4. Mitotic progression of RGCs is significantly impacted in both *Rnu11* cKO and dKO by E12.5. Quantification of the percentage of Aurora B+ mitotic RGCs (Pax6+) across different mitotic phases in control, *Rnu11* cKO, and dKO across E12.5, E13.5, and E14.5. E12.5 control n=5, *Rnu11* cKO n=5, dKO n=5. E13.5 control n=5, *Rnu11* cKO n=5, dKO n=5. E14.5 control n=3, *Rnu11* cKO n=3, dKO n=3. Data are presented as mean±s.e.m. Statistical significance was determined by one-way ANOVA, followed by post-hoc Tukey test.**P<0.01; ***=*P*<0.001. Asterisks color indicates the specific comparison tested for statistical significance, corresponding to the bar color-coding scheme.

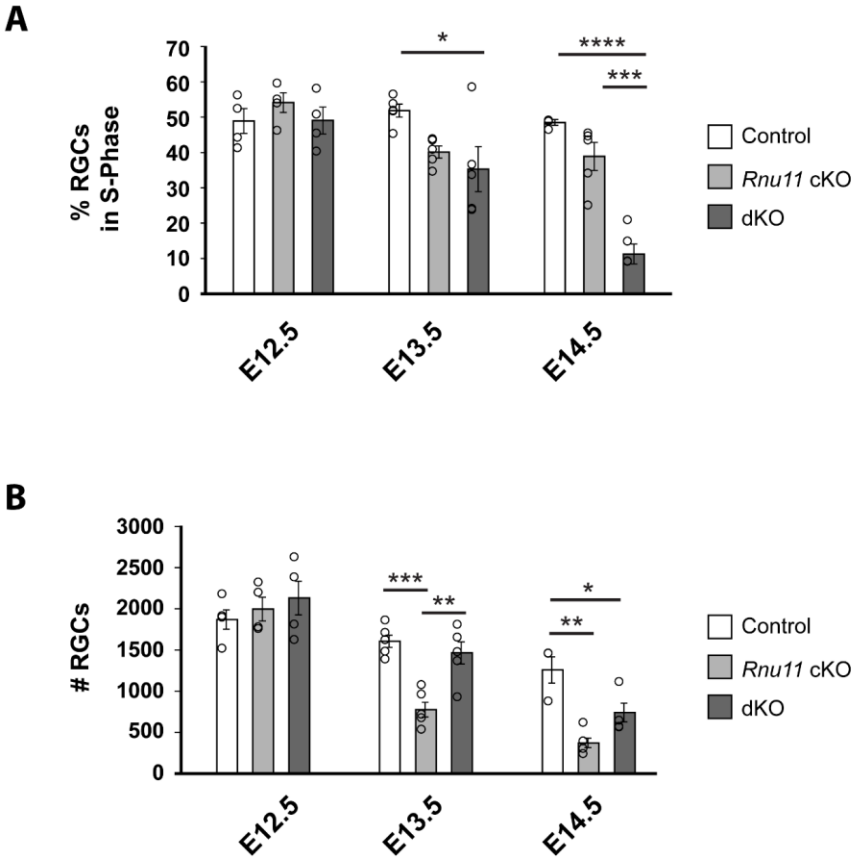

Fig. S5. Radial glial cell number decrease more drastically in Rnu11 cKO, while percentage of radial glial cells in S-phase decreases more in dKO. (A) Quantification of the percentage of RGCs (Pax6+) in S-phase (EdU+) in the control, Rnu11 cKO, and dKO across E12.5, E13.5, and E14.5. **(B)** Quantification of the number of RGCs (Pax6+) in the control, *Rnu11* cKO, and dKO across E12.5, E13.5, and E14.5. E12.5 control n=4, *Rnu11* cKO n=4, dKO n=4. E13.5 control n=5, Rnu11 cKO n=5, dKO n=5. E14.5 control n=3, *Rnu11* cKO n=5, dKO n=4. Data are presented as mean± s.e.m. Statistical significance was determined by one-way ANOVA, followed by post-hoc Tukey test. n.s.=not significant, *=*P*<0.05; **=*P*<0.01; ***=P<0.001; ****=*P*<0.0001.

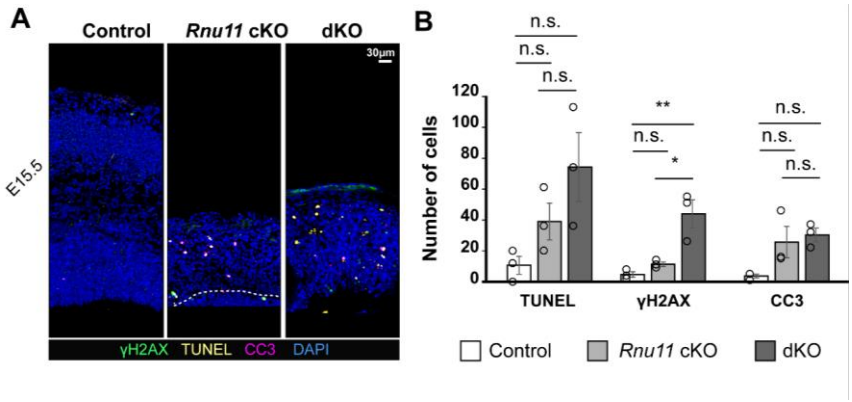

Fig. S6. Delayed DNA damage accumulation observed at E15.5 in the dKO. (A) Immunohistochemistry (IHC) for γH2AX (green), CC3 (magenta), and TUNEL (yellow) on sagittal sections of control (left), *Rnu11* cKO (middle), and dKO (right) pallium at E15.5. Nuclei are marked by DAPI (blue). Scale bar=30μm. (B) Quantification of cell death and DNA damage via TUNEL (left), γH2AX (middle) and CC3 (right) signal in control, *Rnu11* cKO, and dKO at E15.5. Data are presented as mean± s.e.m. Statistical significance was determined by one-way ANOVA, followed by post-hoc Tukey test. n.s.=not significant, *=*P*<0.05; **=*P*<0.01.

Table S1. Table of TPM values from control, *Rnu11* cKO and dKO for selected genes

	Gene	Control TPM	*Rnu11* cKO TPM	dKO TPM
Pallium	*Emx1*	8.840293947	7.237883495	6.045675746
	Lhx2	28.64967879	24.5528281	23.74895361
Non-Pallium	*Dbx1*	0.032800829	0.060871714	0.220381874
	Lhx6	0.34898662	0.799130226	0.294539249
Genetics	*Rnu11*	640.4990113	144.4745943	163.7871724
	Trp53	3.816097869	4.242525529	1.224716406
Intrinsic apoptotic signaling pathway in response to DNA damage by p53 class mediator	*Pmaip1*	0.101162399	1.192623503	0.287988119
	Cdkn1a	0.596901326	3.614278321	0.42530794
	Phlda3	0.501715272	3.459055474	0.42451411
	Bbc3	0.29060454	1.199465547	0.242513608
	Ifi204	0.263741753	1.010334639	0.31668681
	Aen	3.527427918	9.308785941	2.879524064
	Pycard	0.924388152	2.374927478	0.93438391

Table S2. Table of primers used for alternative splicing detection via RT-PCR in Figure 3

Gene	Primer
Dctn3	AACGATGGCGGCTCTGACCGAT
	TCATTCCTCTGCTGGCTTCACTTGC
Nup107	GCAGTCAAAGAGTTGCAAGGTTCTAGG
	AAGGCTGTCGAAAGGAGCTTGGC
Zfp207	GCTTCTTTCCGCCTCTATTCTGCC
	GGTGCTGTATAAGGATCTTCTCATCATC

Table S3. Statistical tests

Click here to download Table S3